

# Capturing nonlinear time-dependent aircraft dynamics using a wind tunnel manoeuvre rig

---

## **Abstract**

This paper considers a novel multi-degree-of-freedom dynamic manoeuvre rig, with the aim of assessing its potential for capturing aircraft model nonlinear time dependent dynamics in the wind tunnel. The dynamic manoeuvre rig capabilities are demonstrated via a series of experiments involving a model aircraft in a closed section low-speed wind tunnel. A series of open loop experiments show that the aircraft model exhibits nonlinear time dependent dynamics. This nonlinear behaviour manifests itself as limit cycle oscillations that increase in complexity with the number of degrees-of-freedom in which the aircraft is allowed to move. Two real-time closed loop control experiments further illustrate the manoeuvre rig potential: first, using a pitch motion configuration, an experiment is conducted to investigate the limit cycle behaviour in more detail, allowing the stability properties of the pitch oscillations to be assessed; secondly, using a 5-DOF motion configuration, the test motion envelope is extended by using a compensating feedback control law to track the aircraft's roll motion. Together, these experiments demonstrate the manoeuvre rig potential to reveal aircraft nonlinear and unsteady phenomena.

*Keywords:* wind tunnel, dynamic testing, limit cycle oscillations, bifurcations, nonlinear dynamics, aerodynamic hysteresis

---

## 1. Introduction

Since the 1920's, wind tunnel dynamic testing has been recognised as an essential tool for flight dynamics. Ever since, the challenge has been to capture the behaviour of a model of the aircraft while mounted in the tunnel. As an early example, in 1922, a continuous rotation balance was developed by Relf and Lander at the Royal Aircraft Establishment in the UK, first for measuring rolling moment [37] and then both the pitching and yawing moments due to angular velocity of roll [21]. Another example is the work by Nicolaides and Eikenberry who measured the static and dynamic aerodynamic characteristics of statically stable and unstable missiles using two free oscillating rigs, a 1-Degree-of-Freedom (DOF) pitch motion rig and a 3-DOF roll, pitch and yaw motion rig [28]. In 1981, Orlik-Ruckemann presented a review of the existing wind tunnel techniques for determining dynamic stability parameters [29], including both unconstrained models capable of providing thrust in free-flight and, more commonly, models that have no thrust capability and hence require constraints. More recently, Huang and Wang presented a summary of the historic development of dynamic testing techniques and reported the state of the art capabilities of dynamic wind tunnel rigs [16], concluding that novel constraining mechanisms that allow the model to have multi-DOF motions have the potential to significantly enhance capabilities for dynamic testing.

Concentrating on captive models, a forced oscillation rig has been used at the 14'  $\times$  22' subsonic wind tunnel at NASA Langley Research Center to study how unsteady aerodynamics affect aircraft flight dynamics [5] and then to estimate the unsteady aerodynamic parameters [24] of a 10% scale F-16XL model. Using the techniques developed for fighter aircraft, research has been carried out

26 to characterise the non-linear and unsteady aerodynamic effects of large transport  
27 aircraft in conditions beyond the normal operating envelope [10, 11, 13, 19, 23,  
28 25, 26, 34, 41]. Modelling of post-stall flight dynamics and spin dynamics of large  
29 transport aeroplanes using data obtained from static, forced oscillation and rotary  
30 balance wind tunnel experiments has been performed by NASA [23]. Moreover,  
31 using static and forced oscillation wind tunnel experiments, a mathematical model  
32 which describes the longitudinal dynamics [25] and the lateral-directional dynam-  
33 ics [26] was produced. Owens *et al.* provided an overview of the dynamic testing  
34 facilities available at NASA Langley Research Centre [30].

35 More recently, the lift and drag forces of a generic unmanned combat air ve-  
36 hicle were characterised using static and forced oscillation testing and then com-  
37 pared to CFD results by Cummings *et al.* working at the Department of Aero-  
38 nautics at the USAF [9]. In the Central Aerohydrodynamic Institute (TsAGI) in  
39 Russia, wind tunnel experiments were carried out to investigate the effect of icing  
40 on the longitudinal steady and unsteady aerodynamic characteristics of an aircraft  
41 model [17]. In the Lu Shijia Laboratory at the Beihang University in China, the  
42 aerodynamic characteristics of a delta wing at high angles of attack were studied  
43 through pitching oscillation experiments in a water channel [51]. In the German-  
44 Dutch Wind Tunnels, a novel dynamic testing rig known as the Model Positioning  
45 Mechanism (MPM) was developed for standard static testing, ground effect sim-  
46 ulation, manoeuvre simulation and forced oscillation testing. The MPM allows  
47 for 6-DOF motions of model aircraft rigidly mounted to a sting and has been used  
48 to identify dynamic derivatives [35] and to simulate complex manoeuvres of a  
49 X-31 model [36]. It has also allowed the deployment trajectories of rigid bodies  
50 launched from a generic military transport aircraft model to be identified [22] and

51 for static and forced oscillation testing of a generic swept wing unmanned com-  
52 bat air vehicle [39, 46–50]. A rig developed at Cranfield University allows for  
53 dynamic testing of aircraft models in roll, pitch, yaw and vertical translation and  
54 has been used to study the stability and control characteristics of a 1/12 scale BAe  
55 Hawk model for small amplitude motions [7, 8]. Most of these techniques are  
56 used for aerodynamic characterisation utilising a relatively low number of DOF.  
57 This results in a need for complementary wind tunnel techniques for multi-DOF  
58 aerodynamic characterisation and flight control law development and evaluation.

59 At the University of Bristol (UoB), the ‘manoeuvre rig’ has been developed  
60 specifically to extend ground testing capabilities for effective flight characteristics  
61 prediction, control law design and evaluation and increased wind-tunnel testing  
62 productivity. Using the rig, the model is attached via a gimbal to an arm which  
63 itself is attached to ground via a second gimbal. It allows the aircraft model to be  
64 tested in up to five degrees of freedom with motions imparted via its own control  
65 surfaces, and with an aerodynamically-driven compensation unit attached to the  
66 rig arm. This unit allows forced oscillation tests and the potential for dynamic  
67 compensation of the rig motions so that the model can behave, in principle, as  
68 if it were in free motion under those DOFs. The resulting ‘physical simulation’  
69 allows for the observation of aircraft behaviour, including the influence of non-  
70 linear and/or time-dependent aerodynamics such as that responsible for the onset  
71 of upset/departure; and the motion data from such tests – or from forced motions  
72 driven by the rig compensator system – can then be used to carry out parameter  
73 estimation for mathematical model development. A similar 5-DOF rig has been  
74 developed at IIT Kanpur to simulate free flight manoeuvres of a delta-winged air-  
75 craft model in a wind tunnel and to estimate simulation model parameters ([33]).

76 In this paper, using the manoeuvre rig as a case study, we discuss the potential  
77 experimental investigations that such rigs allow and how nonlinear time dependent  
78 flight dynamics can be observed. After presenting the rig and broadly discussing  
79 its capabilities in Section 2, we build on previous work obtaining aerodynamic  
80 data [31] and characterising the oscillatory longitudinal pitch and heave motions  
81 of an aircraft model [32] by demonstrating how equilibria and limit-cycle oscilla-  
82 tions (LCO) in heave and pitch can be identified along with the separatrix between  
83 solution types (Section 3). We demonstrate that the robustness of such oscillations  
84 as further DOFs are added can be investigated and reveal that for the aircraft model  
85 investigated there is a strong pitch-roll coupling (Section 4). Section 5 discusses  
86 the potential insights than can be gained when 5 DOF are unlocked and looks at  
87 the use of compensating feedback control laws for tracking roll motion. This dis-  
88 cussion is then extended to consider the potential for using force measurements to  
89 further enhance its control. Finally, Section 6 provides concluding remarks.

## 90 **2. Experimental Platform**

91 In discussing the potential of dynamic testing of captive models in the wind  
92 tunnel, we select the UoB manoeuvre rig as a case-study test facility and consider  
93 the types of testing that can be conducted, giving some example results. In this  
94 section we introduce the manoeuvre rig and then overview the types of testing it,  
95 and similar rigs, can be used for and the insights these can provide.

96 Using the manoeuvre rig the aircraft model is supported on a 3-DOF gimbal,  
97 the model gimbal, which can allow roll, pitch and yaw motions relative to the  
98 gimbal mount. This gimbal is attached to an arm which itself is mounted – via  
99 another 3-DOF gimbal, the arm gimbal – on a fixed vertical strut bolted to a rigid

100 structure below the tunnel working section floor. This arm gimbal provides arm  
101 roll, arm pitch and arm yaw (see Figure 1a). The arm pitch and arm yaw pro-  
102 vide approximate aircraft heave and aircraft sway motions as shown in Figures  
103 2d to 2f. Note that due to the finite arm length, the model gimbal moves in an  
104 arc; this contributes kinematic coupling between the rig motions and those of the  
105 aircraft model. The 3-DOF model gimbal sits at the upstream end of the arm (see  
106 Figure 1a), with the rig compensator located at the downstream end. This gim-  
107 bal connects the arm to the aircraft and allows for aircraft roll, aircraft pitch and  
108 aircraft yaw, as shown in Figures 2a to 2c. Whilst both gimbals incorporate roll  
109 degrees of freedom, they rotate about different axes: the model body axis for the  
110 arm gimbal and arm longitudinal axis for the arm gimbal; the latter will make  
111 additional contributions to the roll and yaw components of rotation in model body  
112 axes. Despite the availability of six rig DOFs, these are considered to imbue the  
113 model itself with a maximum of 5 DOFs: there is no unconstrained fore-aft model  
114 degree of freedom (its translations in this sense are components of motion along  
115 the spherical surface prescribed by arm rotations in yaw and pitch). Note that the  
116 gimbals allow for motions about individual axes to be locked so that the rig can  
117 be configured with DOFs ranging from zero (static) to five.

118 An approximate BAe Hawk aircraft model was used to carry out the experi-  
119 ments presented in this paper. A representation of the Hawk model mounted on  
120 the manoeuvre rig can be seen in Figure 1a. Figure 1b shows the rig when installed  
121 in the  $7' \times 5'$  closed section wind tunnel. A safety cable system can be observed  
122 in the background: this is used to restrict the rig's sway and heave motions.

123 The 3-DOF arm gimbal angular displacements are measured using poten-  
124 tiometers, while those of the 3-DOF model gimbal and the control surfaces from

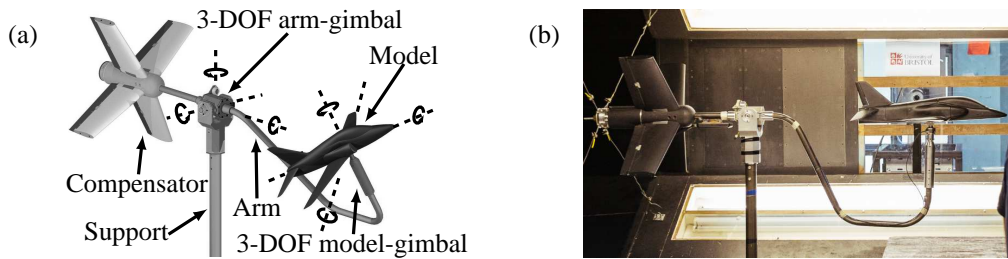


Figure 1: The University of Bristol's manoeuvre rig: (a) 6-DOF manoeuvre rig schematic and (b) rig mounted in the 7' × 5' closed section wind tunnel.

125 the compensator are measured using absolute digital encoders. The aircraft ori-  
 126 entation relative to tunnel (Earth) axes can also be obtained from an inertial mea-  
 127 surement unit (IMU) mounted in the aircraft model. The angular displacements  
 128 of the aircraft model control surfaces are measured using the potentiometers em-  
 129 bedded in the servo motors. The characteristics of the rig and aircraft, kinematic  
 130 equations and dynamic model have been reported previously [1, 3, 27, 31].

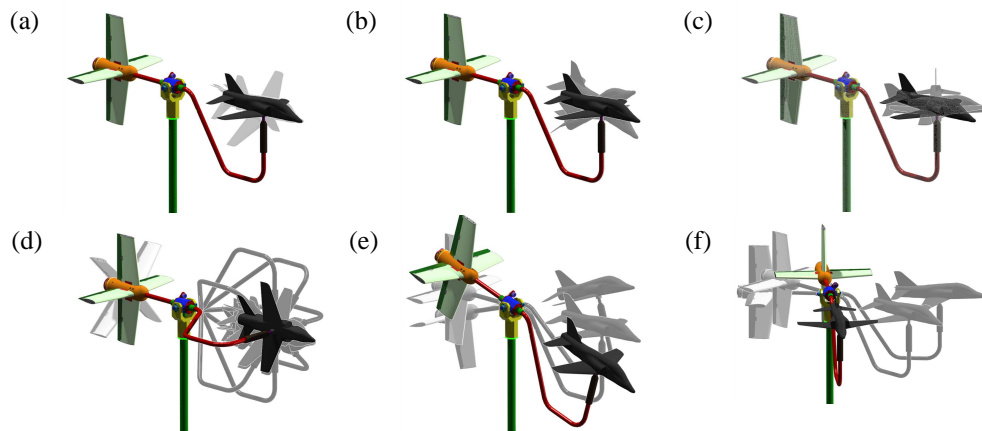


Figure 2: Manoeuvre rig 6-DOF motions: (a) aircraft roll, (b) aircraft pitch, (c) aircraft yaw, (d) aircraft extended roll, (e) aircraft heave and (f) aircraft sway.

131 The rig can be used for various types of testing, which are classified for con-

132 venience as follows.

133 *Rotational DOFs only; model gimbal free with arm gimbal locked:*

- 134 • This can range from 1-DOF to 3-DOF, depending which model gimbal axes  
135 are locked and which are free. Motions are driven by aircraft model control  
136 surfaces or potentially by an external disturbance such as a gust generator.  
137 Note that forced-oscillation experiments can be conducted using the model  
138 control surfaces to acquire dynamic stability derivatives [6, 43], as well as  
139 unsteady aerodynamic characteristics [17].
- 140 • A single-DOF pitch-only test is often a useful starting point for dynamic  
141 testing: motions reflect the approximate short period mode for a conven-  
142 tional aircraft model configuration. Using all 3 DOFs reveals behaviour  
143 indicative of the ‘fast’ modes (short period, Dutch roll, roll subsidence).
- 144 • Tests can examine stability of the modes and, where roll and/or yaw are  
145 free along with pitch, indicate asymmetry and coupling of longitudinal with  
146 lateral-directional dynamics. This can be done by ‘flying’ the model with  
147 random or specified control surface inputs and recording the responses –  
148 so-called ‘physical simulation’.
- 149 • Aerodynamic models providing dependence of loads on  $\alpha$ ,  $\beta$  and rotation  
150 rates can be derived using parameter estimation.
- 151 • Angular rate and stability augmentation controllers can be implemented,  
152 evaluated and tuned.
- 153 • If a load cell is incorporated into the rig, between the end of the arm and  
154 the aircraft gimbal mount, then static and dynamic lift coefficients can be



155 measured about different equilibrium (trim) points.

156 *Rotational DOFs only; model gimbal rotational DoFs free with arm gimbal*  
157 *unlocked in roll:*

- 158 • The arm and gimbals are designed so that the axis of arm rotation in roll  
159 passes through the model gimbal centre; therefore, freeing this degree of  
160 freedom, in addition to any of the model-gimbal DOFs, provides an addi-  
161 tional rotation – about the arm axis – and no associated translation of the  
162 model. This does not add any further DOFs over and above those of the  
163 model gimbal but, importantly, the arm can rotate continuously whereas the  
164 model-gimbal rotation in roll is constrained by hard limits ( $\pm 42^\circ$  at zero  
165 pitch angle). Video 01 (see supplementary material) shows a 3-DOF exam-  
166 ple experiment in which the aircraft is free to move in roll, pitch, and yaw,  
167 with the motion driven by its control surfaces. The manoeuvre rig tracks  
168 the roll motion using feedback control to extend the aircraft’s roll motion  
169 envelope.
  
- 170 • In this configuration, the rig compensator control surfaces can be used to  
171 drive the arm roll (forced rotation/oscillation); alternatively, where model  
172 control surfaces are used to drive model motions, the compensator must be  
173 used to provide for roll responses larger than the model gimbal limits. This  
174 is explored in Section 5.
  
- 175 • Physical simulation, aerodynamic model parameter estimation and control  
176 law evaluation can all be conducted as in the rotation-only tests (with the  
177 additional option of forced motion in roll via the compensator). Similarly,

178 if a load cell is fitted between the arm and model gimbal then force and mo-  
179 ment measurements can be made. An example of this is shown in Video 02  
180 (see supplementary material), where the rig is set-up in a 5-DOF configura-  
181 tion, i.e. aircraft roll, pitch, yaw and approximate heave and sway motions,  
182 with extended rig-roll motion. In this case the aircraft control surfaces drive  
183 the motion, while the aerodynamic compensator is used to compensate the  
184 rig roll dynamics via feedback control.

185 *Rotational and translational DOFs, model and arm gimbals unlocked in at*  
186 *least one DOF:*

187 The same types of testing as above can be conducted, with one or both ‘trans-  
188 lational’ DOFs free, namely model heave through arm pitch and model sway  
189 through arm yaw. The latter introduce further options for compensator-forced  
190 model motions or rig compensation. Application of rig compensation requires  
191 measurement of the reaction force between the aircraft model and the rig arm (via  
192 a load cell); the effect of rig geometric constraints, kinematics and inertial effects  
193 (and in principle also aerodynamic and structural dynamics) on the rig-aircraft dy-  
194 namics are then minimised by feeding back the reaction force to the aerodynamic  
195 compensator [27].

196 • A 2-DOF test with model-gimbal pitch and arm pitch allows a closer ap-  
197 proximation to the short period dynamics of a free aircraft model than rota-  
198 tion only. It also allows for separate estimation of  $\dot{\alpha}$  and  $q$  stability deriva-  
199 tives. Furthermore, even without a load cell, static lift loads can be esti-  
200 mated through the compensator model when the latter is used to balance the  
201 system [15]. When the model is driven by its onboard control surfaces or ex-  
202 cited by an external device such as a gust generator, the compensator can be

203 used to apply compensation for the influence of the rig on model behaviour  
204 or alternatively to force model motions (e.g. for parameter estimation).

205 • A 2-DOF test with model-gimbal yaw and arm sway mirrors the above in  
206 the lateral-directional sense.

207 • All the aforementioned configurations can be combined to form various 2-,  
208 3-, 4- and 5-DOF test condition. The more degrees of freedom given to  
209 the system, the more representative the coupling between longitudinal and  
210 lateral-directional motions and the closer the responses to that of a free-  
211 flying model – including the onset of phenomena such as stall asymmetry  
212 and upset. As before, the behaviour of the aircraft model can be explored  
213 by physical simulation and parameter estimation, control law design, etc.  
214 carried out.

215 Recent applications of the rig have been aimed at assessing the level of in-  
216 teraction between the different DOF as nonlinear phenomena appear, exploring  
217 the compensation of roll motion using the aerodynamic compensator (Figure 1a)  
218 [3], investigating aerodynamic hysteresis utilising a feedback control law to track  
219 the aircraft's equilibria [15] and studying the effects of geometric constraints on  
220 the coupled rig/aircraft dynamics by feedback of load cell reaction force measure-  
221 ments to the compensator control surfaces [27].

222 Next, Sections 3 and 4 present experimental results exploring nonlinear time  
223 dependent flight dynamics and how these dynamics differ as different DOF con-  
224 figurations are used.

### 225 **3. Aircraft Pitch Equilibria and Limit Cycle Oscillations**

226 This section presents results from experiments carried out to explore the LCO  
227 behaviour in a 1-DOF aircraft pitch configuration. Such tests can reveal the influ-  
228 ence of complex flow phenomena on longitudinal behaviour, including changes in  
229 stability, associated bifurcation phenomena leading to LCO and resulting hystere-  
230 sis effects. Similar 1-DOF tests have been carried out before (e.g. [32]) but this  
231 was prior to the rig refinements which provide more accurate measurements of  
232 control surface angles and model rotation rates, hence allowing a more thorough  
233 study. Then, building on these results, the investigation is extended with a series  
234 of tests where a feedback control law is used to study the stability characteristics  
235 of the equilibria and LCO.

236 Pitch LCO for this aircraft model were first reported by Kyle [20], where a  
237 pendulum rig in a 1-DOF pitch motion configuration was used to study the dy-  
238 namics of the aircraft model. The LCO behaviour was modelled by Davison [12]  
239 using hyperbolic tangent growth/decay functions to transition from/to equilibria  
240 and sinusoidal functions to model the shape of the LCO. Subsequently, using the  
241 earlier manoeuvre rig configuration<sup>1</sup> in 1-DOF and 2-DOF configurations, analy-  
242 sis and modelling of the LCO behaviour was carried out by Pattinson using con-  
243 tinuation and bifurcation tools [32]. This involved the identification of parameters  
244 in an unsteady aerodynamic model, along with a friction model, incorporated in  
245 the equations of motion so as to provide as close a match as possible to the limit  
246 cycle characteristics and bifurcationary structure observed in the experiments.

---

<sup>1</sup>This configuration did not provide direct measurements of the model control surfaces and rotational rates (and the aircraft gimbal was 2-DOF rather than 3-DOF).

247 More recently, experimental exploration of the LCO behaviour using an up-  
248 dated version of the manoeuvre rig was carried out [3]. These experiments were  
249 conducted to further explore the lateral-directional interaction between the differ-  
250 ent degrees of freedom as nonlinear phenomena appear (first observed by Pattin-  
251 son *et al* [31], despite the absence of direct measurements of the model aileron  
252  $\delta_{ail}^m$ , elevator  $\delta_{ele}^m$  and rudder  $\delta_{rdd}^m$  or rotation rates  $p_m, q_m, r_m$ ) and to explore roll  
253 motion compensation using the aerodynamic compensator control surfaces.

254 All the results presented throughout this paper are from experiments carried  
255 out in the  $7' \times 5'$  closed circuit wind tunnel at the University of Bristol at a wind  
256 speed of 30 m/s. It will be shown that the rig refinements and incorporation of  
257 feedback control methods provide improved results than in previous studies: in  
258 particular, the effects of unsteady flow phenomena are able to be observed in more  
259 detail, including separatrices between stable solutions and a more complex LCO  
260 structure.

### 261 3.1. 1-DOF Aircraft Pitch LCO

262 First consider the configuration in which the aircraft is free to move in pitch  
263 and the arm is locked in its horizontal position, i.e. the 1-DOF aircraft pitch con-  
264 figuration (Figure 2b). Figure 3a shows the response of the Hawk model in the  
265 time domain when the elevator angle demand is ramped slowly from zero to  $-28^\circ$   
266 and then back to zero. This is a logical first step in this type of testing, where a  
267 control surface is used to provide inputs to model motion: the response to a suf-  
268 ficiently slow ramp-type input can be regarded as quasi-steady and the measured  
269 results are therefore able to be presented both as time histories and in a less usual  
270 format – an experimental bifurcation diagram.

271 The elevator response  $\delta_{ele}^m$  is shown in Figure 3a(i), with the aircraft pitch angle

272  $\theta_m$  and the pitch rate  $q_m$  shown in Figures 3a(ii) and 3a(iii), respectively. Note that  
273 in this 1-DOF configuration,  $\theta_m$  is the model angle of attack. Five regions where  
274 pitch LCO occur can be identified by studying the  $\theta_m$  and  $q_m$  plots, namely in the  
275 periods  $t \approx 50$  s,  $t \approx 100$  s,  $120$  s  $\leq t \leq 180$  s,  $300$  s  $\leq t \leq 350$  s and  $t \approx 400$  s. In  
276 the following discussion the first and fifth of these regions will be referred to as  
277 low  $\alpha$  LCO, and the second, third and fourth regions as high  $\alpha$  LCO. The aircraft  
278 high  $\alpha$  LCO response while in this configuration is presented in the supplementary  
279 video file Video 03.

280 An alternative way of studying the LCO behaviour is by presenting the system  
281 steady state dynamics in the form a bifurcation diagram. Note that equilibrium  
282 (fixed-point) solutions shown in bifurcation diagrams may be regarded as trim-  
283 ming points [17]. For an overview on bifurcation theory and its application to  
284 aircraft dynamics analysis the reader is referred to Goman *et al* [14], Thompson  
285 and Macmillen (eds.) [45] and Sharma *et al* [42]. Using the data shown in Fig-  
286 ure 3a, the aircraft elevator is taken as the bifurcation parameter. Taking only the  
287 points where  $|q_m| \leq 5^\circ/\text{s}$ , i.e. where the rate can be thought of as approximately  
288 the zero-rate points, an experimental bifurcation diagram is obtained as shown in  
289 Figure 3b. Here, the data points represent stable equilibria or limit cycle minimum  
290 and maximum amplitudes. By applying a smoothing post-processing lag-free fil-  
291 ter to this data, some of the features of the LCO are easier to observe. This is  
292 shown in Figure 3c. The filter used here was formulated by Jategaonkar and it is  
293 based on a 15-point symmetric low-pass digital filter developed by Spencer [18].  
294 In Figures 3b and 3c data in blue represent values corresponding to a decreasing  
295 aircraft elevator  $\delta_{ele}^m$  sweep, while data in red represents values corresponding to  
296 an increasing one. The black solid line represents stable equilibria while the black

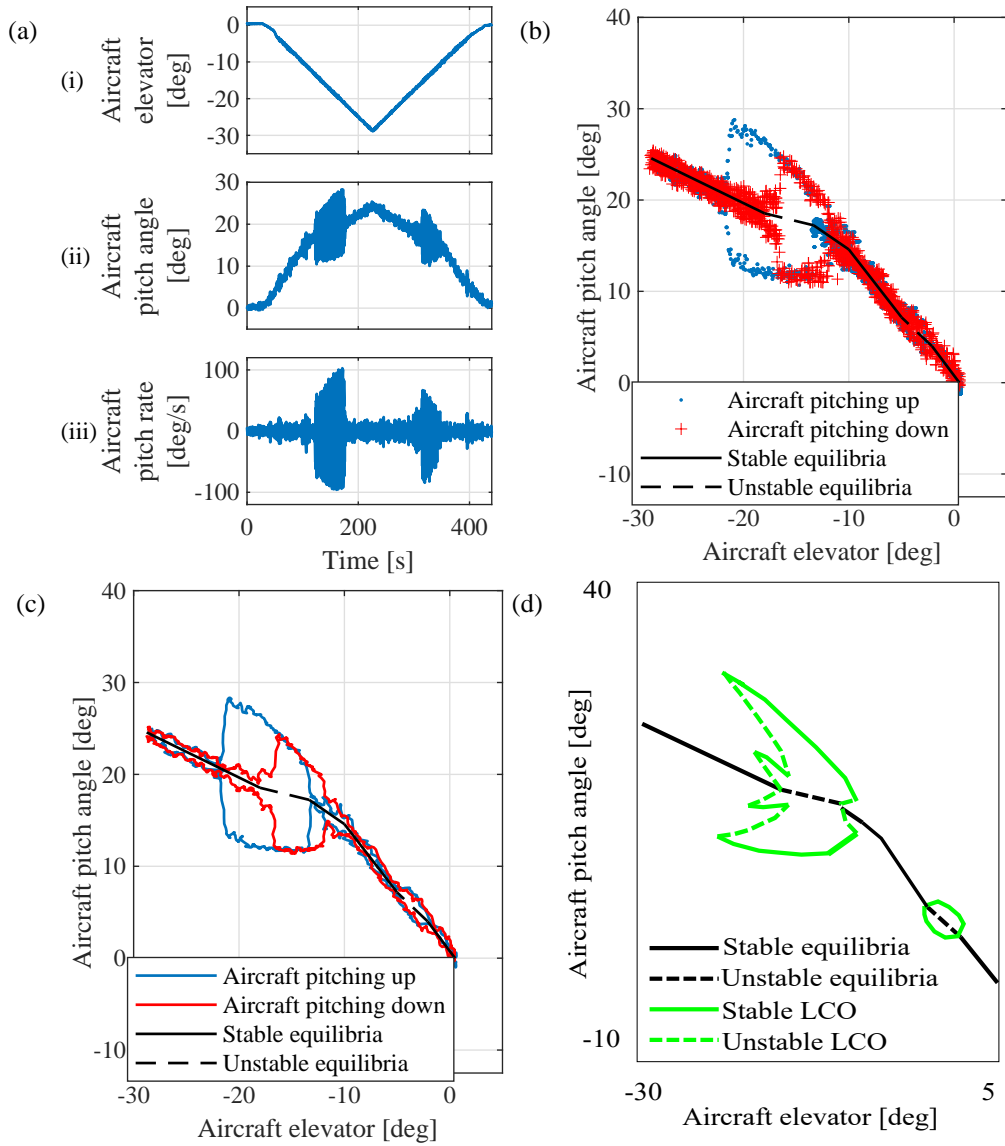


Figure 3: 1-DOF aircraft model pitch experimental data: (a) time histories, (b) point cloud bifurcation diagram, (c) smoothed bifurcation diagram and (d) likely structure of bifurcation diagram.

297 dashed line represents unstable equilibria; these illustrative lines were superim-  
298 posed onto the experimental data to aid its interpretation (no attempt was made in  
299 this work to determine the unstable solutions experimentally).

300 The first of these features is a small LCO at low  $\alpha$  over the region  $-5^\circ \leq \delta_{ele}^m \leq -2^\circ$   
301 and  $3^\circ \leq \theta_{ele} \leq 7^\circ$ , corresponding to those observed around  $t \approx 50$  s and  $t \approx 400$  s  
302 in Figure 3a. The second LCO, the high  $\alpha$  LCO, can be observed over the re-  
303 gion  $-22^\circ \leq \delta_{ele}^m \leq -10^\circ$ . Aerodynamic hysteretic behaviour exhibited by the air-  
304 craft model used for this test can be observed over the region  $-22^\circ \leq \delta_{ele}^m \leq -16^\circ$   
305 and  $-13^\circ \leq \delta_{ele}^m \leq -11.5^\circ$ . In this region the large amplitude LCO is only ob-  
306 served during the decreasing elevator deflection part of the test. When studying in  
307 greater detail the plot corresponding to the aircraft elevator increasing deflection  
308 in the region  $-18^\circ \leq \delta_{ele}^m \leq -16^\circ$ , evidence of an ‘inner’ LCO can be observed.  
309 The characteristics of this LCO are discussed in Section 3.2. Note that the inner  
310 limit cycle might extend further in the pitching up direction due to hysteresis. It  
311 would be possible to investigate this by switching the experiment to a pitch up  
312 ramp at the point where this solution is reached and then following it, but this was  
313 not part of the testing schedule for this study.

314 Based on the features described before, the likely structure of the bifurcation  
315 diagram is sketched in Figure 3d. The sketch shows five features: stable equilibria  
316 in solid black line, unstable equilibria in dashed black line, stable LCO branches  
317 in solid green line (at low and high  $\alpha$ ), high  $\alpha$  unstable LCO branches in dashed  
318 green line and a stable inner branch also in solid green line.

319 The two LCO regions — one around  $\theta = 5^\circ$  (low  $\alpha$ ) and the other starting  
320 at  $\theta = 15^\circ$  (high  $\alpha$ ) — have been reported before [12, 20, 32]. However, a new  
321 feature has been identified here: the results suggest the existence of an inner LCO



322 within the hysteretic region of the high  $\alpha$  LCO. The hysteresis phenomena in  
323 this region were studied in [15] and found to be associated with an asymmetric  
324 separated flow structure on the wings. It was shown in [1], by testing at non-  
325 zero model yaw angles, that this hysteretic behaviour is sustained over a range of  
326 sideslip angles (although their extent does vary noticeably); this suggests that the  
327 existence of these structures is robust to the flow conditions but their characteristics  
328 are dependent on them. The low  $\alpha$  LCO, on the other hand, disappears for larger  
329 sideslip conditions, indicating that it may be linked to loss of longitudinal stability  
330 due to shadowing of the tailplane. Results from a similar test but with non-zero  
331 *rig* yaw angles will be shown in Section 4.1.

### 332 3.2. 1-DOF Aircraft Pitch: Equilibria & LCO Stability

333 To investigate the characteristics of the LCO in more detail and to demonstrate  
334 the manoeuvre rig's capabilities for aircraft control law design and aerodynamic  
335 modelling, a series of closed loop tests using the Hawk model installed on the  
336 manoeuvre rig in a 1-DOF model pitch configuration were performed. In these  
337 tests, the Hawk model elevator was used as the control variable. A feedback  
338 control law implemented in Simulink<sup>®</sup> was used to both set the nominal pitch  
339 angle and then stabilise the aircraft pitch motion. A similar method to the one  
340 presented here was used by Gong *et al* [15] to track the equilibria of pitch-only  
341 dynamics. In this work, the test is used to reveal the more complex LCO structures  
342 and the stability characteristics of both the equilibria and LCO. The design of this  
343 feedback control law is summarised as follows.

344 In a 1-DOF pitch configuration, the aircraft angle of attack  $\alpha_m$  is equal to the

345 aircraft pitch angle  $\theta_m$  and the aircraft pitch dynamics can be described by

$$\begin{aligned} (m_m \ell_{z_m}^2 + I_{yy}) \dot{q}_m = & -f(q_m) - m_m g \ell_{z_m} \sin(\theta_m) + \\ & \frac{1}{2} \rho V^2 S_m \bar{c}_m C_M(\theta_m, q_m, \delta_{ele}^m) + w(t) \end{aligned} \quad (1)$$

346 where  $m_m$  is the aircraft model mass,  $\ell_{z_m}$  is the (small) vertical offset of the model  
 347 centre of gravity (CG) from the gimbal centre of rotation,  $I_{yy}$  is the pitch moment  
 348 of inertia of the model about its CG,  $\dot{q}$  the pitch acceleration,  $f(q_m)$  the model  
 349 gimbal pitch friction,  $g$  the acceleration due to gravity,  $\rho$  the air density,  $V$  the wind  
 350 speed,  $S_m$  and  $\bar{c}_m$  the aircraft model wing reference area and mean aerodynamic  
 351 chord respectively,  $C_M$  the aerodynamic pitching moment coefficient and  $w(t)$  the  
 352 moment contribution due to wind tunnel turbulence.

353 Additionally, considering the aerodynamic pitching moment coefficient as a  
 354 combination of linearly independent functions, gives

$$C_M(\theta_m, q_m, \delta_{ele}^m) = C_{M_0}(\theta_m) + C_{M_{q_m}}(\theta_m, q_m) + C_{M_{\delta_{ele}^m}}(\theta_m, \delta_{ele}^m) \quad (2)$$

355 Here,  $C_{M_{q_m}}$  and  $C_{M_{\delta_{ele}^m}}$  capture the dependence of  $C_M$  on  $q_m$  and  $\delta_{ele}^m$  respectively.

356 Then, by collecting terms, equation (1) can be reformulated as

$$(m_m \ell_{z_m}^2 + I_{yy}) \dot{q}_m = g(\theta_m) + h(\theta_m, q_m) + u(\theta_m, \delta_{ele}^m) + w(t) \quad (3)$$

357 where

$$\begin{aligned}
& \text{Stiffness} \left\{ \begin{aligned} g(\theta_m) &= \frac{1}{2} \rho V^2 S_m \bar{c}_m C_{M_0}(\theta_m) - m_m g \ell_{z_m} \sin(\theta_m) \end{aligned} \right. \\
& \text{Damping} \left\{ \begin{aligned} h(\theta_m, q_m) &= \frac{1}{2} \rho V^2 S_m \bar{c}_m C_{M_{q_m}}(\theta_m, q_m) - f(q_m) \end{aligned} \right. \\
& \text{Control input} \left\{ \begin{aligned} u(\theta_m, \delta_{ele}^m) &= \frac{1}{2} \rho V^2 S_m \bar{c}_m C_{M_{\delta_{ele}^m}}(\theta_m, \delta_{ele}^m) \quad . \end{aligned} \right.
\end{aligned}$$

358 By substituting  $q_m = 0$  and  $\dot{q}_m = 0$  into equation (3) and neglecting any wind  
359 tunnel turbulence, the equilibria of the system can be expressed as

$$u(\bar{\theta}_m, \bar{\delta}_{ele}^m) = -g(\bar{\theta}_m) \quad (4)$$

360 where the over bar indicates equilibrium values. From (4) it can be deduced that,  
361 in the absence of external perturbations, any given aircraft model elevator deflec-  
362 tion results in an equilibrium aircraft pitch angle.

363 Hence, tracking of the equilibria is achieved by defining the control law

$$u(\theta_m, \delta_{ele}^m) = u(\hat{\delta}_{ele}^m) + k_{q_m} q_m \quad (5)$$

364 where  $\hat{\delta}_{ele}^m$  is the aircraft model elevator deflection demand. The term  $k_{q_m} q_m$  in  
365 equation (5) effectively acts as a damper, with  $k_{q_m}$  chosen experimentally such  
366 that any external perturbation is sufficiently damped out.

367 Using the control law defined in (5) and with  $k_{q_m} = 0.1 \text{ N m s/rad}$ , the stability  
368 characteristics of the equilibria, in the regions covering both the inner and outer  
369 high  $\alpha$  LCO, were studied using a total of eleven nominal elevator positions within  
370  $-21^\circ \leq \hat{\delta}_{ele}^m \leq -12^\circ$ . Results for two of these tests are presented in detail followed  
371 by a discussion of all the tests.

372 Figure 4a shows the aircraft model 1-DOF pitch limit cycle suppression time  
 373 histories and phase portraits for a nominal input of  $\hat{\delta}_{ele}^m \approx -15^\circ$ . Subfigures 4ai to  
 374 4aiii show the time histories for the aircraft model elevator, pitch angle and pitch  
 375 rate, respectively. Three sections are of interest: first with the controller off a pitch  
 376 LCO can be observed in the region  $-8.6 \text{ s} \leq t \leq 0 \text{ s}$ . The controller is switched on  
 377 and the LCO is suppressed using the elevator in the region  $0 \text{ s} \leq t \leq 7.4 \text{ s}$ . Lastly,  
 378 in the region  $7.4 \text{ s} \leq t \leq 16.4 \text{ s}$  the controller is switched off and both the pitch  
 379 angle and pitch rate start increasing until they reach the LCO, indicating that the  
 380 equilibrium point is unstable.

381 Figures 4aiv to 4avi show the aircraft model pitch angle and pitch rate phase  
 382 portraits for time segments  $-8.6 \text{ s} \leq t \leq -1.6 \text{ s}$ ,  $3.4 \text{ s} \leq t \leq 7.4 \text{ s}$  and  $7.4 \text{ s} \leq t \leq 16.4 \text{ s}$ ,  
 383 respectively. A fully developed pitch LCO can be observed in Figure 4aiv, with  
 384 the magnitudes of the pitch angle and pitch rate ranging over  $12^\circ \leq \theta_m \leq 25^\circ$  and  
 385  $-86^\circ/\text{s} \leq q_m \leq 76^\circ/\text{s}$ , respectively. Figure 4avi shows the controller successfully  
 386 suppressing the pitch LCO, and the aircraft maintaining its position at  $\theta_m \approx 18.6^\circ$ .  
 387 Figure 4avii, shows the controller switched off and the system returning to the  
 388 pitch LCO, indicating that the equilibrium point is unstable.

389 In a similar fashion, Figure 4b shows the aircraft model 1-DOF pitch limit cy-  
 390 cle suppression time histories and phase portraits for a nominal input of  $\hat{\delta}_{ele}^m \approx -17.5^\circ$ .  
 391 At the beginning of this test the controller is switched off and the nominal elevator  
 392 deflection is held constant. Then a series of step inputs are commanded to the air-  
 393 craft elevator to act as perturbations to the system. The characteristics of the first  
 394 and last step inputs are  $\Delta\delta_{ele}^m \approx 4^\circ$  and  $\Delta t \approx 0.3 \text{ s}$  and  $\Delta\delta_{ele}^m \approx 4^\circ$  and  $\Delta t \approx 1.7 \text{ s}$ , re-  
 395 spectively. The time histories for the aircraft model elevator, pitch angle and pitch  
 396 rate are shown in Figures 4bi to 4biii.

397 With the controller switched off, both the pitch angle and pitch rate remain  
398 bounded around the equilibrium point indicating that the equilibrium point is sta-  
399 ble, see Figures 4bii, 4biii and 4biv. Then at  $t \approx 26$  s, an elevator step input acting  
400 as a perturbation is applied and the system oscillates around the equilibrium but  
401 the oscillation is damped down. Figure 4bv shows the corresponding phase plane  
402 representation for this perturbation and a small orbit can be seen, suggesting an  
403 inner LCO. Five additional step inputs are applied with similar results. From this,  
404 we conclude that this inner LCO is unstable.

405 At  $t \approx 65$  s a step input with the same amplitude is applied over a larger du-  
406 ration and the system transitions to a stable outer pitch LCO. Figure 4bvi shows  
407 the aircraft model pitch angle and pitch rate phase portrait corresponding to this  
408 perturbation.

409 The results from this experiment suggest that in the region of  $\theta_m \approx 20^\circ$ , the  
410 aircraft model has at least three solutions: a stable equilibrium point, a unstable  
411 inner LCO and a stable outer LCO.

412 Similar results were obtained for the remaining elevator nominal positions.  
413 An additional test was carried out in which a slow ramp input to the aircraft ele-  
414 vator was commanded while the LCO-suppressing controller was active. This test  
415 allowed the equilibrium points for different elevator deflections to be obtained ex-  
416 perimentally. The data is presented in the form of a bifurcation diagram in Figure  
417 5 using the aircraft elevator as the bifurcation parameter. The experimentally ob-  
418 tained equilibria are shown (red 'x' markers) along with manually computed stable  
419 equilibria (solid black line) and unstable equilibria (dashed black line). It can be  
420 observed that the controller successfully tracked the equilibria, except for the re-  
421 gion  $\theta_m \approx 16^\circ$ . The equilibrium points are unstable in two regions:  $-4^\circ \leq \delta_{ele}^m \leq 0^\circ$

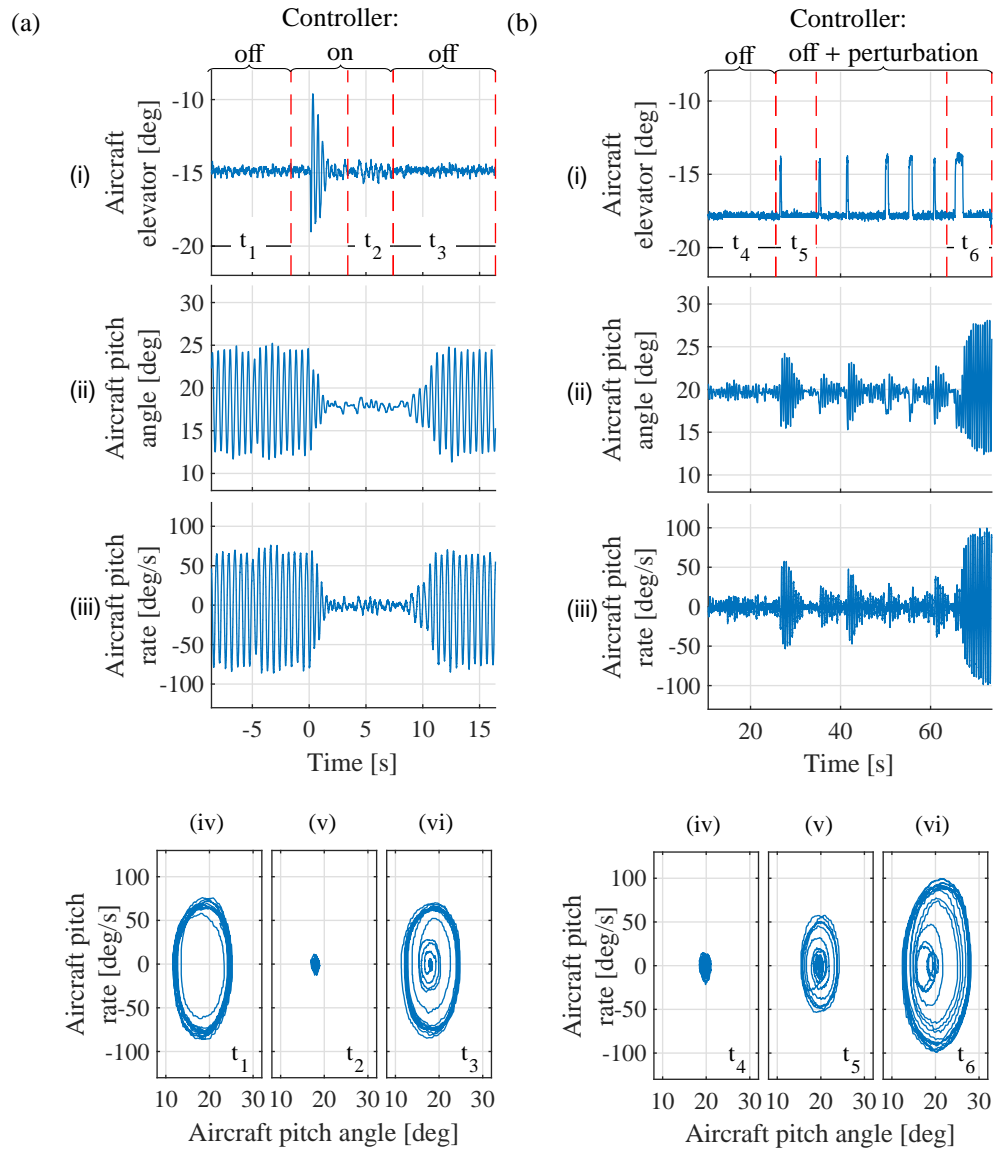


Figure 4: Aircraft model 1-DOF pitch limit cycle suppression time histories and phase portraits:

(a) nominal input  $\hat{\delta}_{ele}^m \approx -15^\circ$  and (b) nominal input  $\hat{\delta}_{ele}^m \approx -17.5^\circ$ .

422 and  $-17^\circ \leq \delta_{ele}^m \leq -11^\circ$ . Around these regions pitch LCO have been found. In the  
 423 region  $-22^\circ \leq \delta_{ele}^m \leq -12^\circ$ , the stable LCO (black line with ‘+’ markers) can be  
 424 seen in Figure 5. Lastly, in the region  $-19^\circ \leq \delta_{ele}^m \leq -16^\circ$ , the unstable LCO is  
 425 shown as a dashed black line with ‘+’ markers. Note that these unstable LCO  
 426 represent the boundary that separates the equilibria from the stable LCO, i.e. the  
 427 separatrix of the system.

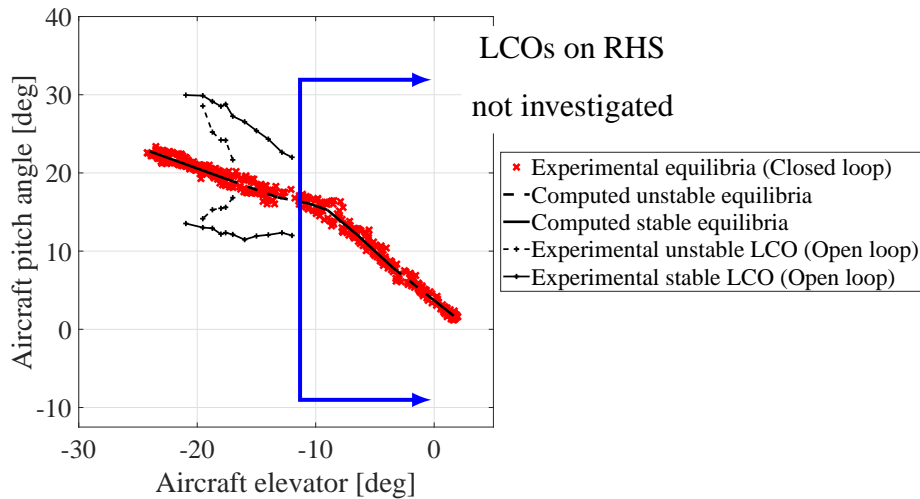


Figure 5: 1-DOF aircraft model pitch experimental bifurcation diagram.

428 The results presented in this section show that the controller successfully sup-  
 429 pressed the LCO behaviour in the 1-DOF aircraft model pitch experiment. The  
 430 all-moving tailplane was able to provide the necessary control power to achieve  
 431 this (the flow over the tailplane is not stalled in this high angle-of-attack region).  
 432 By virtue of this technique, the stability characteristics of the aircraft’s equilibria  
 433 and LCO were determined and the inner unstable LCO has been identified for this  
 434 model for the first time. From a fluid dynamics point of view, the causes behind

435 the observed LCO behaviour are not entirely understood but it is possible that two  
436 flow breakdown structures are involved at high angle of attack, in a similar vein  
437 to the variation in lift hysteresis for the delta wing model in [51]: PIV experi-  
438 ments in a water tunnel tests suggested this behaviour was related to a dual-core  
439 leading-edge vortex phenomenon.

440 Whilst the application here is the sub-scale approximate Hawk aircraft model,  
441 the technique can be applied to any wind tunnel model which has actuated con-  
442 trol effectors, thus enabling similar studies of stability and associated dynamical  
443 structure to be revealed experimentally. The approach can be extended to exploit  
444 the potential of ‘control-based continuation’: a technique for tracking the solu-  
445 tions and bifurcations of nonlinear experiments. It aims to achieve the equivalent  
446 of numerical continuation but applied to a physical experiment, through the use  
447 of ‘minimally invasive’ feedback control schemes – see [38] for an explanation  
448 of the method and [44] for an example of an application to wing aeroelastic re-  
449 sponses in a wind tunnel. A simplified implementation of this technique on the  
450 Hawk model mounted on the manoeuvre rig has revealed additional complexity  
451 in its hysteretic behaviour [15].

#### 452 **4. Robustness of LCOs to Additional DOFs**

453 Releasing additional degrees of freedom in the manoeuvre rig allows for the  
454 study of interaction of longitudinal phenomena, such as the limit cycles and hys-  
455 teresis discussed in the previous section, with lateral-directional dynamics. This  
456 is especially important at higher angles of attack where effects of nonlinearity  
457 typically become relevant and asymmetric responses to symmetric conditions can  
458 occur: it is frequently the case that the development of stall in an aircraft results



459 in roll and/or yaw when no lateral-directional inputs are given.

460 Here, to explore the interaction of the Hawk longitudinal LCO behaviour with  
461 its lateral-directional dynamics and its evolution as different degrees of freedom  
462 are freed up, a series of multi-DOF tests was performed. Using different combi-  
463 nations of model pitch, model yaw, model roll, arm roll and arm yaw degrees of  
464 freedom as appropriate, inputs to the Hawk model elevator, rudder and ailerons  
465 were used to drive the motion of the model. These experimental results are pre-  
466 sented in three parts: firstly a 2-DOF configuration using the aircraft pitch and  
467 yaw DOF is presented, secondly two further 2-DOF configurations, one using the  
468 aircraft model pitch and roll DOF and another using the aircraft model pitch and  
469 arm roll DOF are considered; finally a 4-DOF (no heave) configuration is tested  
470 where compensation of roll motion using the aerodynamic compensator is used to  
471 keep the model gimbal roll angle as close as possible to zero.

#### 472 4.1. 2-DOF Aircraft Pitch & Yaw

473 For the 2-DOF aircraft pitch and aircraft yaw experiments, five different con-  
474 stant inputs to the aircraft elevator were applied, namely  $\delta_{ele}^m = [-2, -5, -10, -15, -20]^\circ$ ,  
475 with a slow ramp applied to the aircraft rudder over the range  $-39^\circ \leq \delta_{rudd}^m \leq 39^\circ$ .

476 Using the time history data from this experiment, 2-DOF bifurcation diagrams  
477 were obtained following the procedure described in Section 3.1. The aircraft rudder  
478 was used as the bifurcation parameter and each aircraft elevator input setting  
479 was treated as an independent data set. The diagrams for  $\delta_{ele}^m = [-2^\circ, -5^\circ, -10^\circ, -15^\circ, -20^\circ]$ ,  
480 are shown in Figures 6a to 6e, respectively. The blue line represents a sweep of  
481 decreasing aircraft rudder  $\delta_{rudd}^m$ , while the red line represents an increasing one.  
482 The black dashed lines represent the system's approximate equilibria. These were

483 computed by taking an average of the values corresponding to the decreasing air-  
484 craft rudder  $\delta_{rdd}^m$  sweep in each case, represented by the blue lines.

485 The analysis of the nonlinear phenomena for this experiment is divided into  
486 two: the low and high  $\alpha$  LCO regions. The 2-DOF bifurcation diagrams for the  
487 first region are shown in Figures 6a and 6b. These show that the low  $\alpha$  LCO  
488 persists throughout the range of tested  $\psi_m$  (unlike in the tests with different *model*  
489 yaw angles – not shown here [1]). Figure 6b shows a small amplitude oscillation in  
490 yaw angle for  $3^\circ \leq \delta_{rdd}^m \leq 27^\circ$ . This suggests that the shadowing of the horizontal  
491 tail by the wing/fuselage, proposed in Section 3.1 as the cause of the low angle-of-  
492 attack LCO, may also affect the fin in this region, indicating a lack of symmetry.  
493 Figures 6c, 6d and 6e coincide with the high  $\alpha$  LCO region. In contrast with the  
494 low  $\alpha$  LCO region, strong interaction between the pitch and yaw dynamics can  
495 be observed. This interaction can be better observed in Figure 6f which shows a  
496 phase portrait for  $\delta_{ele}^m = -15^\circ$ ,  $-6^\circ \leq \delta_{rdd}^m \leq 3^\circ$ . This phase portrait was produced  
497 using data from the segment between the vertical dashed lines in Figure 6d. The  
498 time history for this region shows that the number of orbits of the LCO pitch  
499 component is twice that of the LCO yaw component which indicates that the pitch  
500 component has double the frequency of the yawing motion.

#### 501 4.2. 2-DOF Aircraft Pitch & Roll

502 A series of 2-DOF aircraft roll and pitch experiments was carried out to study  
503 coupled pitch-roll interaction in the regions where LCO behaviour appears. Two  
504 configurations were studied, one encompassing the aircraft roll and pitch DOFs  
505 and a second one using the aircraft pitch and the arm roll DOFs.

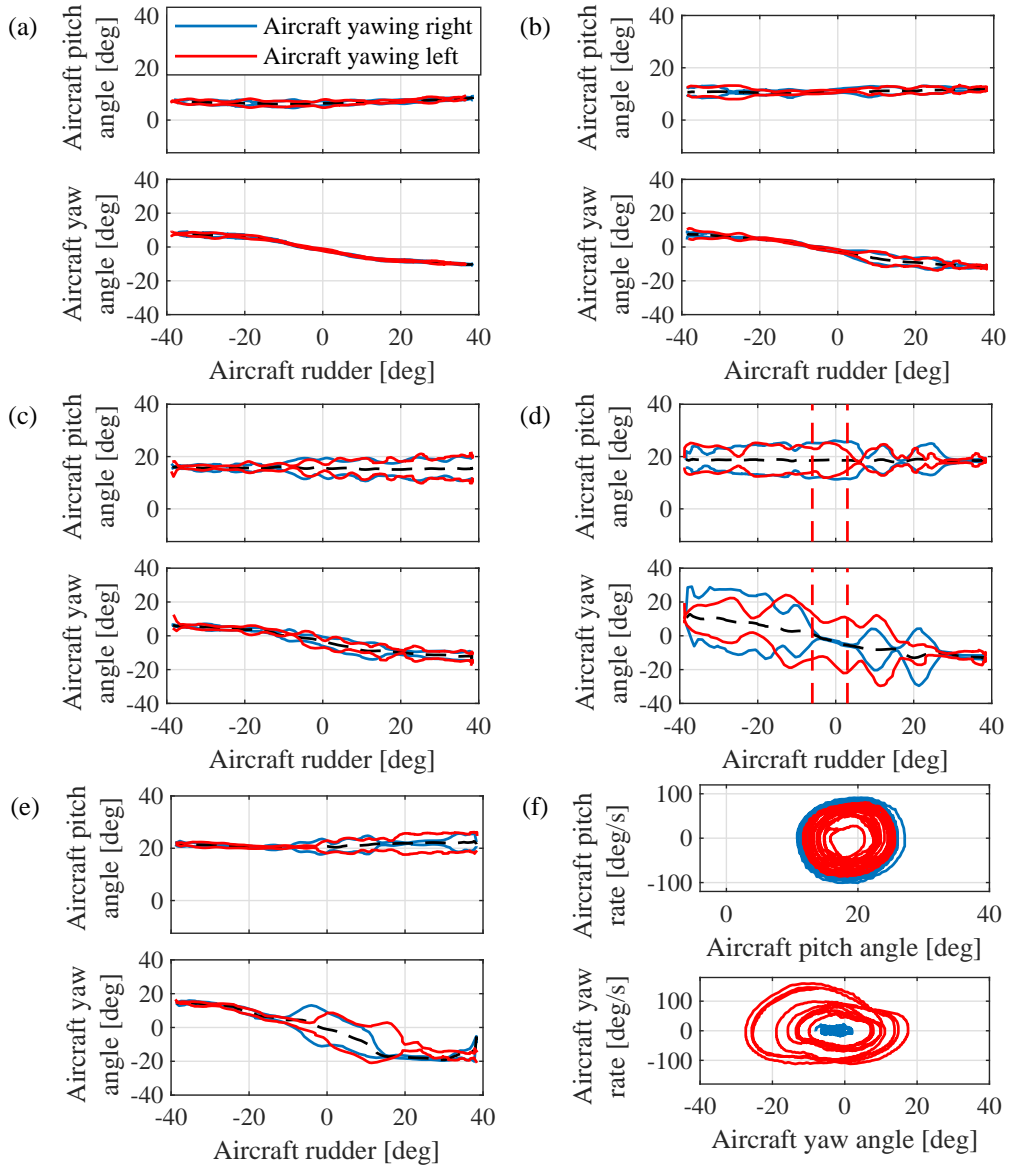


Figure 6: 2-DOF aircraft model pitch & yaw experimental bifurcation diagrams for: (a)  $\delta_{ele}^m = -2^\circ$ , (b)  $\delta_{ele}^m = -5^\circ$ , (c)  $\delta_{ele}^m = -10^\circ$ , (d)  $\delta_{ele}^m = -15^\circ$ , (e)  $\delta_{ele}^m = -20^\circ$  and (f) phase portrait for  $\delta_{ele}^m = -15^\circ$  and  $-6^\circ \leq \delta_{rudd}^m \leq 3^\circ$ .

506 *4.2.1. 2-DOF Aircraft Pitch & Aircraft Roll*

507 In this experiment a slow ramp-and-hold input to the aircraft elevator was ap-  
508 plied and the aircraft roll and pitch motion responses were recorded. It was found  
509 that at  $\theta_m \approx 15^\circ$ , the roll-pitch interaction caused the aircraft to reach the physical  
510 limits of the roll gimbal (approximately  $\pm 38^\circ$ ). As a consequence a reduced range  
511 of pitch motions is presented here.

512 Figure 7a shows the time histories for this experiment, with the aircraft model  
513 elevator deflection, roll angle, pitch angle, roll rate and pitch rate shown in Figures  
514 7ai to 7av, respectively. Note that the range of elevator input is less here than  
515 in Section 3.1 due to the roll gimbal mechanical limits being reached at more  
516 negative elevator settings. In this Figure a pitch LCO at low  $\alpha$  can be seen in the  
517 regions  $35 \text{ s} \leq t \leq 75 \text{ s}$  and  $340 \text{ s} \leq t \leq 380 \text{ s}$ , with a maximum rate of  $54^\circ/\text{s}$ . In  
518 the region  $150 \text{ s} < t < 230 \text{ s}$ , it can be observed that the aircraft experiences roll  
519 oscillations and reaches the roll gimbal limits. When the aircraft elevator angle  
520 starts increasing at  $t \approx 250 \text{ s}$ , the roll oscillations begin to damp down and the  
521 aircraft roll angle goes back to a steady state bounded by  $-10^\circ < \phi_m < 10^\circ$ .

522 The point at which the low- $\alpha$  LCO appears, at  $t \approx 35 \text{ s}$ , and disappears, at  
523  $t \approx 380 \text{ s}$ , is at a higher pitch amplitude than in the 1-DOF case and is accompa-  
524 nied by an offset in average roll angle. This negative roll angle persists through  
525 the LCO and after exiting the LCO at higher  $\alpha$ , i.e. a roll asymmetry exists for all  
526 pitch angles above approx.  $\approx 5^\circ$ . Its existence appears to be linked to the bifurca-  
527 tion giving rise to the LCO, with zero roll angle at lower angles of attack (before  
528 the tailplane becomes immersed in the wing-fuselage wake) and a roll offset when  
529 it is immersed and when it emerges below the wake at higher  $\alpha$ .

530 Figure 7b shows a smoothed experimental 2-DOF bifurcation diagram ob-

531 tained following the procedure described in Section 3.1 by excluding the data  
532 points that correspond to motions where the aircraft reaches its roll gimbal limits.  
533 In this diagram the aircraft elevator is the bifurcation parameter. In Figure 7bii  
534 the ‘jump’ in roll angle that was observed in Figure 7a (at the Hopf bifurcation  
535 point at which the low- $\alpha$  LCO is borne) is evident – at  $\delta_{ele}^m \approx 1^\circ$  when the aircraft  
536 model is pitching up and  $\delta_{ele}^m \approx 2^\circ$  when pitching down. The roll angle is then  
537 more constant at pitch angles above the low  $\alpha$  LCO (observed in Figure 7bi in the  
538 region  $-2^\circ \leq \delta_{ele}^m \leq 3^\circ$ ), although there are changes in value at higher  $\alpha$ .

539 Figure 7c shows a detailed view of the time histories for  $246 \text{ s} \leq t \leq 254 \text{ s}$ .  
540 Roll oscillations can be observed while the elevator deflection is held constant,  
541 which suggest there may exist periodic solutions in this region. Using the data  
542 shown in Figure 7c, a phase portrait diagram was constructed (see Figure 7d).  
543 While the phase portrait shows almost no excitation of the aircraft pitch dynamics,  
544 several orbits can be observed in the roll motion plot, suggesting the possibility  
545 that roll oscillations may drive the onset of the pitch oscillations observed when  
546 the gimbal roll DOF was locked.

547 The results from this experiment confirm the existence of roll-pitch interac-  
548 tion. They suggest that the roll oscillation may delay the onset of pitch oscillations  
549 to higher  $\alpha$ , although the fact that the roll motion hits the gimbal limits makes it  
550 difficult to reach definite conclusions in this respect.

#### 551 4.2.2. 2-DOF Aircraft Pitch & Arm Roll

552 Whilst the above results highlight the potential benefit of adding a roll DOF,  
553 i.e. to explore longitudinal-lateral interaction, they also demonstrated the limita-  
554 tion of relying on an aircraft-mounted gimbal with angular constraints. Here, a  
555 2-DOF aircraft pitch and roll experiment was carried out in similar fashion to the

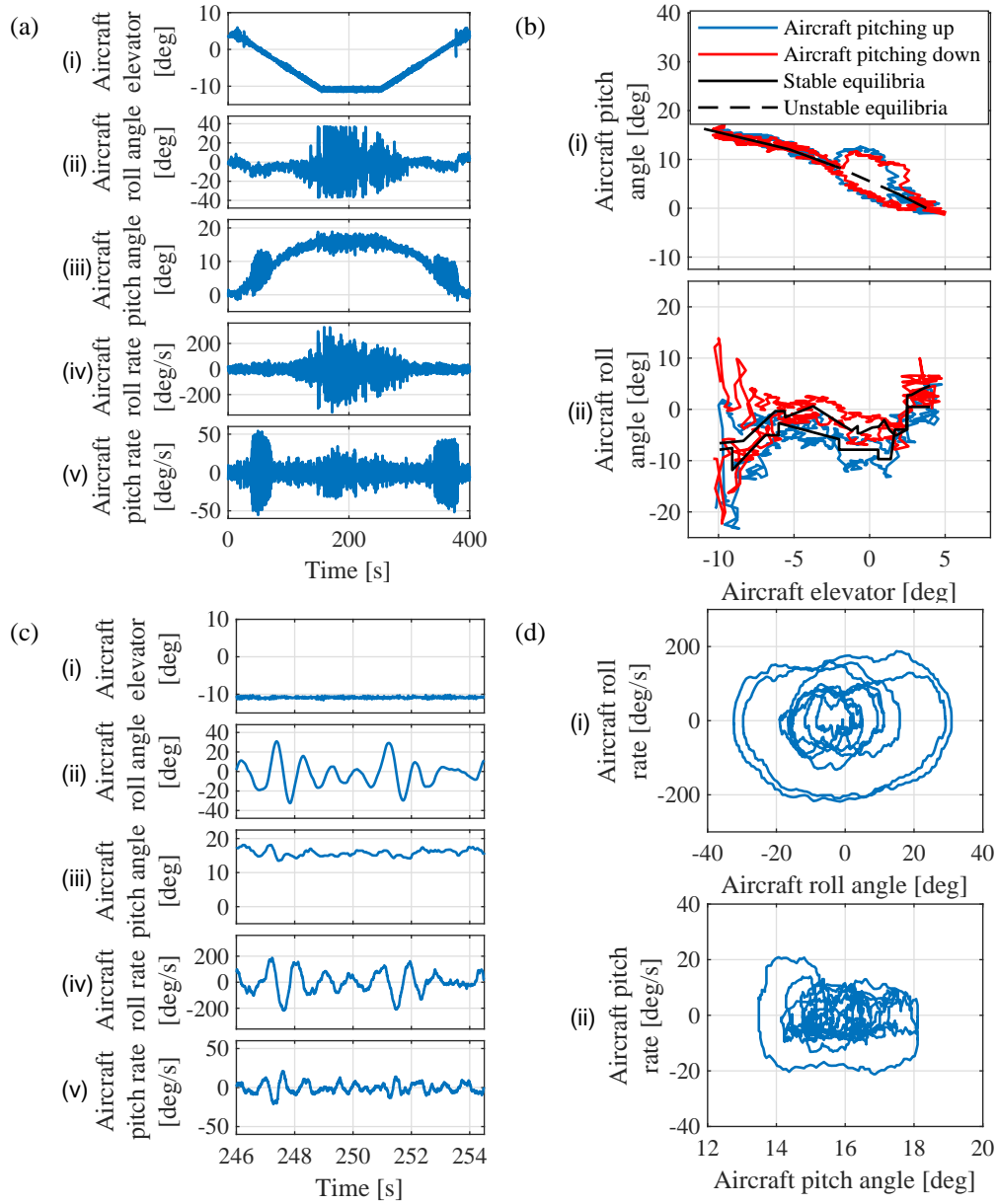


Figure 7: 2-DOF aircraft model roll and pitch experiment: (a) time histories, (b) bifurcation diagram, (c) time histories detailed view and (d) phase portrait diagram.

556 one presented in the previous subsection except that roll was obtained through the  
557 arm gimbal roll rather than the model gimbal: the arm gimbal allows unlimited  
558 motion. A slow ramp input to the aircraft elevator was applied and the aircraft  
559 pitch and arm roll motion responses were recorded.

560 To account for the offset between the Hawk model CG and the arm gimbal  
561 roll axis, the aircraft roll motion was computed using an extended Kalman filter  
562 (EKF) applied to signals from the IMU mounted on the aircraft model. Note that  
563 the influence of this offset is assumed to be negligible when considering rig heave  
564 and sway as it is very small (approx. 14 mm).

565 Figures 8ai, to 8av show the time histories of the aircraft model elevator de-  
566 flection, the aircraft roll angle, pitch angle, roll rate and pitch rate, respectively.  
567 Two LCO can be observed at low and high  $\alpha$  in the regions  $65\text{ s} \leq t \leq 130\text{ s}$ ,  
568  $680\text{ s} \leq t \leq 760\text{ s}$ ,  $200\text{ s} \leq t \leq 330\text{ s}$  and  $500\text{ s} \leq t \leq 620\text{ s}$ , respectively. This is  
569 consistent with the experimental results presented in Sections 3 and 4.1, except  
570 that the onset of the high  $\alpha$  LCO is delayed to a higher angle of attack (approx.  
571  $20^\circ$ ). These LCO are easier to study using the 2-DOF arm roll and aircraft pitch  
572 smoothed bifurcation diagram shown in Figure 8b. The bifurcation diagram was  
573 obtained using the same data processing method as described in Section 3.1 and  
574 using the aircraft elevator as the bifurcation parameter.

575 The low and high  $\alpha$  LCO can be observed in Figure 8bi in the regions  $-3^\circ \leq \delta_{ele}^m \leq 3^\circ$   
576 and  $-9.5^\circ \leq \delta_{ele}^m \leq -23^\circ$ , respectively. In Figure 8bii, it can be observed that  
577 the roll angle decreases proportionally with the aircraft elevator in the regions  
578  $3^\circ < \delta_{ele}^m < 10^\circ$  and  $-9^\circ < \delta_{ele}^m < -3^\circ$ , suggesting lateral dynamics asymmetry. This  
579 behaviour is similar to that observed in the aircraft pitch configuration presented  
580 in Section 4.2.1. The roll angle does appear to vary more smoothly between these

581 two regions, which coincides with the onset of the low  $\alpha$  LCO, without the discrete  
 582 ‘jump’ evident in Figure 7b.

583 The high  $\alpha$  LCO is preceded by oscillations in roll in the region delimited by  
 584  $-12^\circ < \delta_{ele}^m < -9^\circ$ , suggesting that roll oscillations may induce the onset of pitch  
 585 oscillations. It is also noticeable that there is an increase in roll angle amplitude  
 586 when the LCO dies out at higher  $\alpha$  ( $\delta_{ele}^m < -21^\circ$ ).

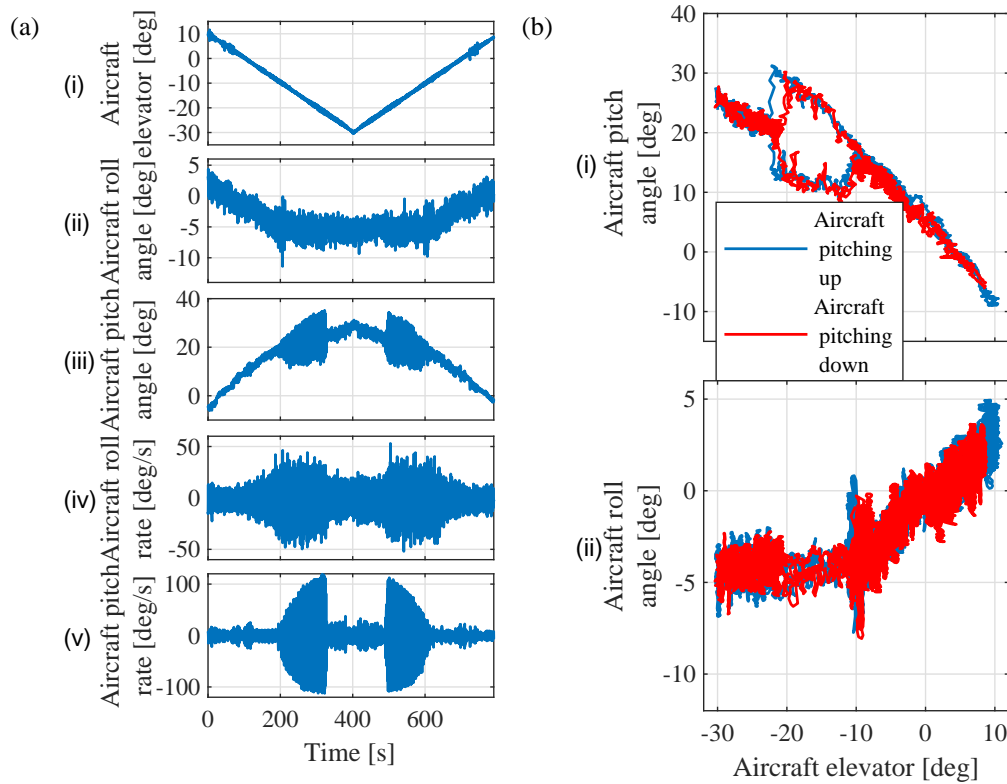


Figure 8: 2-DOF arm roll and aircraft pitch experiment: (a) time histories and (b) bifurcation diagram.

587 When compared with the 1-DOF aircraft pitch experiment two points are  
 588 worth noting. Firstly, the low  $\alpha$  LCO seems to be completely driven by lon-



589 gitudinal effects. Secondly, the roll-pitch interaction in the high  $\alpha$  LCO is strong  
590 enough to change the shape of the hysteretic behaviour region (around  $\delta_{ele}^m = -10^\circ$   
591 to  $-12^\circ$ ), almost to the point of making it disappear. This suggests that, in this re-  
592 gion, the onset of the pitch oscillations may be induced by the roll dynamics.

593 The results from this experiment indicate that there is strong roll-pitch inter-  
594 action throughout the test space. This interaction is observed in the form of arm  
595 roll deflection. Given the inertia and pendulum effect of the arm, this arm roll  
596 deflection suggests the existence of significant rolling moments induced by the  
597 aircraft on the rig arm. Clearly, this configuration has the disadvantage of the air-  
598 craft model dynamic response being modified by the effects of arm inertia and the  
599 offset of the rig CG from the roll axis. Whilst this can be accounted for in pro-  
600 cessing results, it does preclude correct physical simulation of an aircraft model  
601 that has no constraints on motion in its degrees of freedom. On the other hand,  
602 when testing under the approximate free-to-roll conditions afforded by the model  
603 gimbal roll DOF, the envelope within which physical simulation could be carried  
604 out is constrained by the roll gimbal limits (as seen in Section 4.2.1). In the case  
605 of the Hawk model, if it were free to roll without gimbal limits and without rig in-  
606 ertial effects, it is likely that the roll-pitch interaction would lead to more complex  
607 behaviour such as wing rock and/or wing drop. Therefore, in the next section, we  
608 exploit the rig compensator to attempt to eliminate the influence of the rig arm on  
609 the model roll dynamics.

## 610 **5. Compensation of Rig Dynamics**

611 A 4-DOF experiment was carried out to study the open loop behaviour of the  
612 aircraft model in a multi-DOF configuration where only the arm gimbal pitch DOF

613 was locked, such that the aircraft is unable to heave. It is however able to pitch,  
614 yaw, roll (both via the aircraft and the arm gimbals) and sway. In this experiment, a  
615 flight control stick was used to manually control the aircraft ailerons and elevator.  
616 The rig arm roll motion was controlled via the aerodynamic control surfaces on  
617 the compensator (referred to as compensator ailerons), using a control law with  
618 feedback of model roll rate and roll angle relative to the arm. The control objective  
619 was to track the aircraft's roll motion, keeping the model gimbal roll angle as close  
620 as possible to zero. Here, the model gimbal roll DOF, with its low inertial load,  
621 can be thought of as allowing for fast aircraft roll dynamics while the arm roll  
622 DOF allows slow dynamics over the full  $360^\circ$  range.

623 Figure 9 shows the aircraft model motion time histories, with panels ai to aiii  
624 showing the control inputs and the rest the aircraft model motion variables. The  
625 control inputs consist of:

- 626 • compensator aileron deflection (actively controlled),  $\delta_{ail}^c$ , Figure 9ai,
- 627 • aircraft model aileron deflection,  $\delta_{ail}^m$ , Figure 9aai and
- 628 • aircraft model elevator deflection,  $\delta_{ele}^m$ , Figure 9aaii.

629 The aircraft model motion variables are:

- 630 • roll rate,  $p_m$ , Figure 9aiv,
- 631 • pitch rate,  $q_m$ , Figure 9av,
- 632 • yaw rate,  $r_m$ , Figure 9avi,
- 633 • angle of attack,  $\alpha_m$  (blue solid line), and pitch angle,  $\theta_m$  (red dashed line),  
634 shown in Figure 9avii,

- 635 • angle of sideslip,  $\beta_m$  (blue solid line), and yaw angle,  $\psi_m$  (red dashed line),  
636 shown in Figure 9aviii,
- 637 • roll angle,  $\phi_m$ , shown in Figure 9aix and
- 638 • aircraft gimbal roll angle,  $\phi_g$ , shown in Figure 9ax.

639 Figure 9b shows a magnification of 9a. The aircraft angles of attack and sideslip  
640 were computed off-line using the arm gimbal angles, the model gimbal angles and  
641 the aircraft rotational rates. The equations used to compute these can be found in  
642 Araujo-Estrada [1].

643 With the aircraft in an initial trimmed state, the aircraft elevator is slowly de-  
644 creased to increase the aircraft angle of attack (see Figures 9aiii and 9avii). Two  
645 segments are of interest. Firstly, in the region  $2 \text{ s} \leq t \leq 15 \text{ s}$ , the low  $\alpha$  pitch LCO  
646 previously identified can be observed (Figures 9av and 9avii). In keeping with  
647 the previous 2-DOF tests (Section 4), there seems to be little interaction between  
648 the aircraft pitch motion and the remaining DOFs, for which time histories show  
649 relatively small magnitude changes.

650 Secondly, more complex behaviour involving all the DOFs can be observed in  
651 the region  $19 \text{ s} \leq t \leq 30 \text{ s}$ . At  $t \approx 19 \text{ s}$ , an increase in the rolling moment and side  
652 force is experienced by the aircraft (manifested via the  $\psi_m$  and  $\phi_m$  time histories  
653 in Figures 9aviii and 9aix). A manual input to  $\delta_{ail}^m$  is applied to correct  $\phi_m$  (Figure  
654 9aai). After this,  $\delta_{ele}^m$  is decreased further and the system seems to track the equi-  
655 libria. At  $t \approx 25 \text{ s}$ , the aircraft accelerates in roll  $\phi_m$  causing a fast change in the  
656 gimbal roll angle  $\phi_g$ . This rapid change in the dynamics is easier to observe in  
657 Figures 9bix and 9bx. As a consequence, the compensator ailerons deflect (Fig-  
658 ure 9bi), allowing  $|\phi_m| > 100^\circ$  (Figure 9bix), without reaching the gimbal physical

659 limits (Figure 9bx). At  $t \approx 26.8$  s, the aircraft accelerates once more in roll and a  
660 sharp change in  $\phi_g$  is observed. The compensator ailerons deflect to compensate  
661 the roll motion, allowing the aircraft to complete two roll revolutions (Figures  
662 9ai and 9aix), before the aircraft ultimately reaches the gimbal mechanical limits  
663 (Figure 9bx). Finally, the aircraft aileron and elevator stick inputs are released,  
664 and the system returns to a trimmed state.

665 The results from this experiment confirm that there is negligible interaction  
666 between the aircraft pitch motion and the other DOFs in the low  $\alpha$  LCO. Also,  
667 in the region corresponding to the previously identified high  $\alpha$  LCO, complex be-  
668 haviour involving all DOF is observed and the motion response is dominated by  
669 the lateral-directional dynamics. Further insight into the roll asymmetries respon-  
670 sible for the onset of the high- $\alpha$  LCO has been developed in a separate study of  
671 the Hawk model equilibria, using a ‘minimally invasive’ feedback controller, in  
672 a different multi-DOF test [15]. Lastly by controlling the arm roll via the com-  
673 pensator the allowable model roll was increased substantially before the roll rate  
674 results in stops being reached.

675 This 4-DOF test demonstrates the added capability of arm roll tracking com-  
676 pensation in revealing coupled responses of an aircraft model. A complementary  
677 compensation strategy, proposed by Navaratna et. al [27], utilizes a load cell in-  
678 corporated in the rig just below the model gimbal and aims to reduce the influence  
679 of the arm dynamics on the aircraft model motions by feeding back the reaction  
680 force between the aircraft and the rig arm to the aerodynamic compensator. Sim-  
681 ulation results indicate that by using this approach, the aircraft model dynamics  
682 does more closely match equivalent free flight behaviour for various modes of  
683 motion.

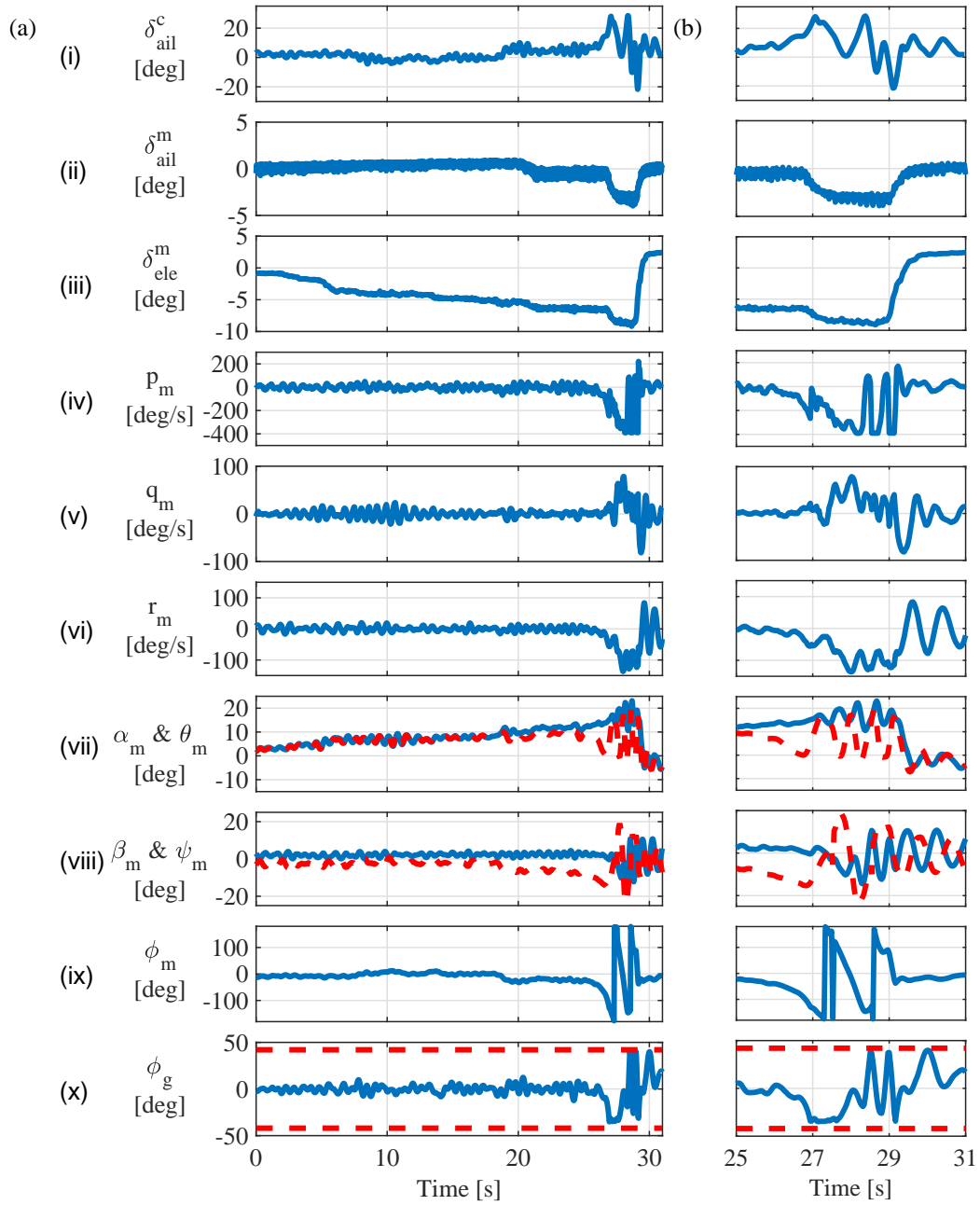


Figure 9: 5-DOF No-heave: (a) aircraft motion time histories and (b) time histories detailed view. Where two lines are plotted, the first listed in the label is plotted as a solid line.

## 684 **6. Concluding Remarks**

685 In this paper, the potential of gaining new insights into aircraft behaviour us-  
686 ing novel wind tunnel manoeuvre rigs is examined. Possible testing regimes are  
687 discussed and, using an approximate BAe Hawk wind tunnel model, example re-  
688 sults and associated insights are presented. Specifically, for the Hawk model, both  
689 open and closed loop tests are used to reveal nonlinear behaviour, which manifests  
690 itself as LCO and were observed in all testing configurations.

691 By releasing the manoeuvre rig DOFs incrementally in open loop experiments  
692 it was possible to observe the evolution of complex dynamic behaviour. First, a 1-  
693 DOF pitch test allowed two main regions where pitch LCO appear to be identified:  
694 one around  $\theta = 5^\circ$  (low  $\alpha$ ) and another starting at  $\theta = 15^\circ$  (high  $\alpha$ ). These results  
695 are in agreement with those previously presented by Kyle [20], Davison [12] and  
696 Pattinson [32]. Additionally, the LCO structure was found to be more complex  
697 than previous tests had suggested, with evidence of an inner LCO within the high  
698  $\alpha$  LCO region. Application of a feedback controller in a 1-DOF model pitch  
699 configuration allowed the stability characteristics of the model equilibria and LCO  
700 to be assessed and allowed the inner unstable LCO within the high  $\alpha$  LCO to be  
701 identified.

702 When a 2-DOF aircraft pitch and yaw configuration was used it was found that  
703 the low  $\alpha$  LCO was dominated by pitch motions. The high  $\alpha$  LCO region is more  
704 complex: both pitch and yaw motions are present with the pitch component hav-  
705 ing twice the frequency of the yaw component. A strong roll-pitch interaction in  
706 the high  $\alpha$  LCO was identified using 2-DOF results from both the aircraft roll and  
707 pitch and the aircraft pitch and arm roll. As a result of the high roll rates induced  
708 by this coupling, limitations arising from motions exceeding gimbal mechanical

709 limits were evident in the case where the model roll gimbal was used. When the  
710 arm roll DOF was deployed instead, revealing the magnitude of the rolling mo-  
711 ment being exerted by the aircraft model on the arm, the impact of arm inertia and  
712 offset CG on the model responses was also highlighted. These roll motion issues  
713 justified the deployment of the rig compensator surfaces in order to allow uncon-  
714 strained model roll motions whilst minimizing rig effects. This was demonstrated  
715 in the last of the experiments reported in the paper, in which feedback control  
716 to the compensator ailerons was implemented in a 4-DOF (roll-pitch-yaw-sway)  
717 configuration. This confirmed the strong roll-pitch coupling characteristics and  
718 allowed the roll testing envelope to increase. However, the model did ultimately  
719 reach its gimbal mechanical limits, thus indicating that the aircraft roll dynamics  
720 are faster than that of the rig arm so that compensation was not fully achieved in  
721 this case.

722 For the Hawk model, the experimental results presented here provide a new  
723 perspective on the nature of what was previously considered to be a pitch-only  
724 LCO in the high  $\alpha$  region, shedding light on the interaction between the longitu-  
725 dinal and lateral-directional dynamics where the LCO appears.

726 More generally, the experiments reported in this paper reveal the capacity of  
727 this novel type of wind tunnel dynamic test rig to physically simulate the motions  
728 of an air vehicle in multiple degrees of freedom, and to use open- and closed-loop  
729 testing to reveal insights into the responses arising from nonlinear and unsteady  
730 aerodynamic effects, including evaluation of stability and hysteresis phenomena.  
731 The nature of this type of rig, where the aircraft model motion is driven by its  
732 own control surfaces, is seen to be particularly well suited to studies of complex  
733 or counter-intuitive behaviours such as in the initiation of aircraft upset/loss-of-

734 control scenarios. Future application of this technique could be used to enhance:  
735 flight characteristics modelling, to develop and evaluate online system identifi-  
736 cation techniques [40], to extract stability derivatives in combination with Ma-  
737 chine Learning methods [43] or to validate CFD simulations of novel aircraft in  
738 subsonic regimes [6]; and for design and evaluation of flight control laws, like  
739 Machine Learning-based attitude controllers for fixed-wing UAVs [4].

## 740 **Acknowledgments**

741 S. A. Araujo-Estrada's research was supported by the Science and Technol-  
742 ogy National Council (CONACYT-Mexico), studentship # 215262. S. Neild was  
743 supported by an EPSRC fellowship (EP/K005375/1). The authors thank Prof.  
744 Mikhail Goman for his insights and suggestions in support of the development  
745 of this rig and the work described in this paper. The authors would like to thank  
746 and acknowledge Mr Lee Winter from the University of Bristol wind tunnel lab-  
747 oratory, for his invaluable support and work during the refitting, assembly and  
748 modification of the equipment used to carry out the experiments presented in this  
749 paper.

## 750 **References**

- 751 [1] S.A. Araujo-Estrada. *Control of a Wind Tunnel Manoeuvre-Rig to Physically*  
752 *Simulate Free-Flight Motion of an Aircraft Model*. PhD thesis, University of  
753 Bristol, Bristol, England, UK, 2016. Department of Aerospace Engineering.
- 754 [2] S.A. Araujo-Estrada, Z. Gong, M.H. Lowenberg, S.A. Neild, and M.G. Go-  
755 man. Wind Tunnel Manoeuvre Rig: A Multi-DOF Test Platform for Model



- 756 Aircraft. In *54th AIAA Aerospace Sciences Meeting*, San Diego, California,  
757 Jan. 2016. AIAA. DOI: 10.2514/6.2016-2119.
- 758 [3] S.A. Araujo-Estrada, M.H. Lowenberg, S.A. Neild, and M.G. Goman. Eval-  
759 uation of Aircraft Model Upset Behaviour Using Wind Tunnel Manoeu-  
760 vre Rig. In *AIAA Atmospheric Flight Mechanics Conference*, Kissimmee,  
761 Florida, Jan. 2015. AIAA. DOI: 10.2514/6.2015-0750.
- 762 [4] E. Bohn, E.M. Coates, S. Moe, and T.A. Johansen. Deep reinforce-  
763 ment learning attitude control of fixed-wing UAVs using proximal pol-  
764 icy optimization. In *2019 International Conference on Unmanned Air-  
765 craft Systems, ICUAS 2019*, Atlanta, Georgia, June 2019. IEEE. DOI:  
766 10.1109/ICUAS.2019.8798254.
- 767 [5] J. Brandon and J. Foster. Recent dynamic measurements and considerations  
768 for aerodynamic modeling of fighter airplane configurations. In *23rd At-  
769 mospheric Flight Mechanics Conference, Guidance, Navigation, and Con-  
770 trol and Co-located Conferences*, Boston, Massachusetts, Aug. 1998. AIAA.  
771 DOI: 10.2514/6.1998-4447.
- 772 [6] T. Bykerk, D. Verstraete, and J. Steelant. Low speed longitudinal dynamic  
773 stability analysis of a hypersonic waverider using unsteady Reynolds aver-  
774 aged Navier Stokes forced oscillation simulations. *Aerospace Science and  
775 Technology*, 103:105883, 2020. DOI: 10.1016/j.ast.2020.105883.
- 776 [7] S. Carnduff, S. Erbsloeh, A. Cooke, and M. Cook. Development of a Low  
777 Cost Dynamic Wind Tunnel Facility Utilizing MEMS Inertial Sensors. In

- 778        *46th AIAA Aerospace Sciences Meeting and Exhibit, Aerospace Sciences*  
779        *Meetings*, Reno, Nevada, Jan. 2008. AIAA. DOI: 10.2514/6.2008-196.
- 780        [8] S.D. Carnduff, S.D. Erbsloeh, A.K. Cooke, and M.V. Cook. Characteriz-  
781        ing Stability and Control of Subscale Aircraft from Wind-Tunnel Dynamic  
782        Motion. *Journal of Aircraft*, 46(1):137–147, 2009. DOI: 10.2514/1.36730.
- 783        [9] R.M. Cummings, S.A. Morton, and S.G. Siegel. Numerical prediction  
784        and wind tunnel experiment for a pitching unmanned combat air vehicle.  
785        *Aerospace Science and Technology*, 12(5):355–364, Jul. 2008.
- 786        [10] K. Cunningham, J.V. Foster, G.H. Shah, E.C. Stewart, R.A. Rivers, J.E.  
787        Wilborn, and W. Gato. Simulation study of a commercial transport airplane  
788        during stall and post-stall flight. In *World Aviation Congress & Exposition*,  
789        Reno, Nevada, November 2004. SAE International. SAE Technical Paper  
790        2004-01-3100, DOI: 10.4271/2004-01-3100.
- 791        [11] K. Cunningham, J. Foster, G. Shah, E. Stewart, R. Ventura, R. Rivers, J.  
792        Wilborn, and W. Gato. Simulation study of flap effects on a commercial  
793        transport airplane in upset conditions. In *Atmospheric Flight Mechanics*  
794        *Conference and Exhibit*, San Francisco, California, Aug. 2005. AIAA. DOI:  
795        10.2514/6.2005-5908.
- 796        [12] P.M. Davison, M.H. Lowenberg and M. di Bernardo. Experimental Analysis  
797        and Modeling of Limit Cycles in a Dynamic Wind-Tunnel Rig. *Journal of*  
798        *Aircraft*, vol. 40, no. 4, pp. 776-785, Jul.-Aug. 2003. DOI: 10.2514/2.3158.
- 799        [13] J. Foster, K. Cunningham, C. Fremaux, G. Shah, E. Stewart, R. Rivers, J.  
800        Wilborn, and W. Gato. Dynamics modeling and simulation of large trans-

- 801 port airplanes in upset conditions. In *Atmospheric Flight Mechanics Con-*  
802 *ference and Exhibit*, San Francisco, California, Aug. 2005. AIAA. DOI:  
803 10.2514/6.2005-5933.
- 804 [14] , M.G. Goman, G.I. Zagainov and A.V. Khramtsovsky. Application  
805 of Bifurcation Methods to Nonlinear Flight Dynamics Problems. *Prog.*  
806 *Aerospace Sci.*, vol. 33, iss. 9-10, pp539-586, 1997. DOI: 10.1016/S0376-  
807 0421(97)00001-8.
- 808 [15] Z. Gong, S. Araujo-Estrada, M.H. Lowenberg, S.A. Neild, and M. G. Go-  
809 man. Experimental Investigation of Aerodynamic Hysteresis Using a Five-  
810 Degree-of-Freedom Wind-Tunnel Maneuver Rig. *Journal of Aircraft*, pages  
811 1–11, Jan. 2019.
- 812 [16] M. Huang and Z.W. Wang. A review of wind tunnel based virtual  
813 flight testing techniques for evaluation of flight control systems. *Inter-*  
814 *national Journal of Aerospace Engineering*, 2015(1):1–22, 2015. DOI:  
815 10.1155/2015/672423.
- 816 [17] D.I. Ignatyev, A.N. and Khrabrov, A.I. Kortukova, D.A. Alieva, M.E. Sido-  
817 ryuk, and S.G. Bazhenov. Interplay of unsteady aerodynamics and flight  
818 dynamics of transport aircraft in icing conditions. *Aerospace Science and*  
819 *Technology*, 104:105914, 2020. DOI: 10.1016/j.ast.2020.105914.
- 820 [18] R.V. Jategaonkar. Flight Vehicle System Identification: A Time Domain  
821 Methodology American Institute of Aeronautics and Astronautics, 2006.  
822 DOI: 10.2514/4.866852.

- 823 [19] T. Jordan, W. Langford, C.M. Belcastro, J. Foster, G. Shah, G. Howland,  
824 and R. Kidd. Development of a dynamically scaled generic transport model  
825 testbed for flight research experiments. NASA technical report, NASA Lan-  
826 gley Research Center, 2004. ID:20040085988.
- 827 [20] H. Kyle. *An investigation into the use of a pendulum support rig for aero-*  
828 *dynamic modelling*. PhD thesis, University of Bristol, Bristol, England, UK,  
829 2004. Department of Aerospace Engineering.
- 830 [21] T. Lavender. A Continuous Rotation Balance for the Measurement of Pitch-  
831 ing and Yawing Moments Due to Angular Velocity of Roll ( $M_p$  and  $N_p$ ).  
832 In *Technical Report of the Aeronautical Research Committee*. ARC1, Feb.  
833 1925. Reports & Memoranda 936.
- 834 [22] T. Löser and A. Bergmann. Capabilities of Deployment Tests at DNW-  
835 NWB. In *Fluid Dynamics of Personnel and Equipment Precision Delivery*  
836 *from Military Platforms*, pages 10–1 – 10–12, Neuilly-sur-Seine, France:  
837 RTO, 2006. AIAA. Meeting Proceedings RTO-MP-AVT-133, Paper 10. (Ac-  
838 cessed: 2016-07-01). [Online]. Available: <https://tinyurl.com/ybdejouz>
- 839 [23] A. Murch and J. Foster. Recent NASA Research on Aerodynamic Model-  
840 ing of Post-Stall and Spin Dynamics of Large Transport Airplanes. In *45th*  
841 *AIAA Aerospace Sciences Meeting and Exhibit, Aerospace Sciences Meet-*  
842 *ings*, Reno, Nevada, Jan. 2007. AIAA. DOI: 10.2514/6.2007-463.
- 843 [24] P. Murphy and V. Klein. Estimation of aircraft unsteady aerodynamic pa-  
844 rameters from dynamic wind tunnel testing. In *AIAA Atmospheric Flight*  
845 *Mechanics Conference and Exhibit, Guidance, Navigation, and Control and*

- 846 *Co-located Conferences*, Montreal, Canada, August 2001. AIAA. DOI:  
847 10.2514/6.2001-4016.
- 848 [25] P. Murphy and V. Klein. Transport aircraft system identification from wind  
849 tunnel data. In *AIAA Atmospheric Flight Mechanics Conference and Exhibit,*  
850 *Guidance, Navigation, and Control and Co-located Conferences*, Honolulu,  
851 Hawaii, August 2008. AIAA. DOI: 10.2514/6.2008-6202.
- 852 [26] P. Murphy and V. Klein. Transport aircraft system identification using roll  
853 and yaw oscillatory wind tunnel data. In *AIAA Atmospheric Flight Me-*  
854 *chanics Conference and Exhibit, Guidance, Navigation, and Control and*  
855 *Co-located Conferences*, Toronto, Canada, August 2010. AIAA. DOI:  
856 10.2514/6.2010-8122.
- 857 [27] P.D.B. Navaratna, M.H. Lowenberg, and S.A. Neild. Minimally Constrained  
858 Flight Simulation in Wind Tunnel. *Journal of Aircraft*, vol. 56, no. 4, Jul.  
859 2019. DOI: 10.2514/1.C035199.
- 860 [28] J.D. Nicolaides and R.S. Eikenberry. Dynamic wind tunnel testing tech-  
861 niques. In *AIAA Aerodynamic Testing Conference*, Los Angeles, California,  
862 September 1966. AIAA. DOI: 10.2514/6.1966-752.
- 863 [29] K. Orlik-Ruckemann. Review of Techniques for Determination of Dynamic  
864 Stability Parameters in Wind Tunnels. In *Dynamic Stability Parameters,*  
865 *Lecture Series, LS-114*, California, USA and Rhode-Saint-Genese, Belgium,  
866 March 1981. Advisory Group for Aerospace Research and Development  
867 (AGARD). Paper 3.

- 868 [30] B. Owens, J. Brandon, M. Croom, M. Fremaux, G. Heim, and D. Vicroy.  
869 Overview of dynamic test techniques for flight dynamics research at NASA  
870 LaRC. In *25th AIAA Aerodynamic Measurement Technology and Ground*  
871 *Testing Conference, Fluid Dynamics and Co-located Conferences*, San Fran-  
872 cisco, California, June 2006. AIAA. DOI: 10.2514/6.2006-3146.
- 873 [31] J. Pattinson, M.H. Lowenberg and M.G. Goman. Multi-Degree-of-Freedom  
874 Wind-Tunnel Maneuver Rig for Dynamic Simulation and Aerodynamic  
875 Model Identification. *Journal of Aircraft*, vol. 50, no. 2, pp. 551-566, Mar.-  
876 Apr. 2013. DOI: 10.2514/1.C031924.
- 877 [32] J. Pattinson, M.H. Lowenberg and M.G. Goman. Investigation of Poststall  
878 Pitch Oscillations of an Aircraft Wind-Tunnel Model. *Journal of Aircraft*,  
879 vol. 50, no. 6, pp. 1843-1855, Nov.-Dec. 2013. DOI: 10.2514/1.C032184.
- 880 [33] N. K. Peyada, A. K. Ghosh, and T. H. Go. Mathematical modelling, sim-  
881 ulation, and estimation of aircraft parameters using five degree-of-freedom  
882 dynamic test rig. *Proceedings of the Institution of Mechanical Engineers,*  
883 *Part G: Journal of Aerospace Engineering*, 226(1):55–63, 2012. DOI:  
884 10.1177/0954410011407265.
- 885 [34] J. Foster, K. Cunningham, C. Fremaux, G. Shah, E. Stewart, R. Rivers, J.  
886 Wilborn, and W. Gato. High-incidence stabilator as an out-of-control re-  
887 covery device for a fixed-wing subscale transport unmanned air vehicle. In  
888 *43rd AIAA Aerospace Sciences Meeting and Exhibit*, Reno, Nevada, January  
889 2005. AIAA. DOI: 10.2514/6.2005-1022.
- 890 [35] M. Rein, G. Höhler, A. Schütte, A. Bergmann, and T. Löser. Ground-

- 891 Based Simulation of Complex Maneuvers of a Delta-Wing Aircraft. In *25th*  
892 *AIAA Aerodynamic Measurement Technology and Ground Testing Confer-*  
893 *ence, Fluid Dynamics and Co-located Conferences*, San Francisco, Califor-  
894 nia, June 2006. AIAA. DOI: 10.2514/6.2006-3149.
- 895 [36] M. Rein, G. Höhler, A. Schütte, A. Bergmann, and T. Löser. Ground-Based  
896 Simulation of Complex Maneuvers of a Delta-Wing Aircraft. *Journal of*  
897 *Aircraft*, 45(1):286–291, 2008. DOI: 10.2514/1.30033.
- 898 [37] E. Relf and T. Lavender. A Continuous Rotation Balance for the Measure-  
899 ment of  $L_p$  at Small Rates of Roll. In *Technical Report of the Aeronautical*  
900 *Research Committee*. ARC, August 1922. Reports & Memoranda 828.
- 901 [38] L. Renson, A.D. Shaw, D.A.W. Barton, S.A. Neild. Application of control-  
902 based continuation to a nonlinear structure with harmonically coupled  
903 modes. *Mechanical Systems and Signal Processing*, vol. 120, pp449-464,  
904 2019. DOI: 10.1016/j.ymssp.2018.10.008.
- 905 [39] D. Rohlf, S. Schmidt, and J. Irving. SACCON Stability and Control Anal-  
906 yses Applying System Identification Techniques. In *28th AIAA Applied*  
907 *Aerodynamics Conference, Fluid Dynamics and Co-located Conferences*,  
908 Chicago, Illinois, June 2010. AIAA. DOI: 10.2514/6.2010-4399.
- 909 [40] G. Seo, Y. Kim, and S. Saderla. Kalman-filter based online system iden-  
910 tification of fixed-wing aircraft in upset condition. *Aerospace Science and*  
911 *Technology*, 89:307–317, 2019. DOI: 10.1016/j.ast.2019.04.012.
- 912 [41] G.H. Shah, K. Cunningham, J.V. Foster, C.M. Fremaux, E.C. Stewart, J.E.  
913 Wilborn, W. Gato, and D.W. Pratt. Wind-tunnel investigation of commercial

- 914 transport aircraft aerodynamics at extreme flight conditions. In *World Avia-*  
915 *tion Congress & Display*, Phoenix, Arizona, November 2002. SAE Interna-  
916 tional. SAE Technical Paper 2002-01-2912, DOI: 10.4271/2002-01-2912.
- 917 [42] S. Sharma, E. Coetzee, M. Lowenberg, S. Neild and B. Krauskopf. Numer-  
918 ical continuation and bifurcation analysis in aircraft design: an industrial  
919 perspective. *Philosophical Transactions of the Royal Society A*, vol. 373,  
920 iss. 2051, Sep. 2015. DOI: 10.1098/rsta.2014.0406.
- 921 [43] M. Tatar, and M. Masdari. Investigation of pitch damping derivatives  
922 for the Standard Dynamic Model at high angles of attack using neural  
923 network. *Aerospace Science and Technology*, 92:685–695, 2019. DOI:  
924 10.1016/j.ast.2019.06.046.
- 925 [44] I. Tartaruga, D.A.W. Barton, D. Rezgui and S.A. Neild. Experimental bifur-  
926 cation analysis of a wing profile. Paper presented at International Forum on  
927 Aeroelasticity and Structural Dynamics, IFASD-2019-155, Savannah, US,  
928 June 2019.
- 929 [45] J.M.T. Thompson and F.B.J. Macmillen (Eds.). *Nonlinear Flight Dynamics*  
930 *of High-Performance Aircraft*. *Phil. Trans. R. Soc. Lon. A*, vol. 356, no.  
931 1745”, Oct. 1998. DOI: 10.1098/rsta.1998.0267.
- 932 [46] T. Loeser, D. Vicroy, and A. Schuette. SACCON Static Wind Tunnel Tests  
933 at DNW-NWB and 14' × 22' NASA LaRC. In *28th AIAA Applied Aerody-*  
934 *namics Conference, Fluid Dynamics and Co-located Conferences*, Chicago,  
935 Illinois, June 2010. AIAA. DOI: 10.2514/6.2010-4393.



- 936 [47] D. Vicroy, T. Loeser, and A. Schütte. SACCON Dynamic Wind Tunnel Tests  
937 at DNW-NWB and 14' × 22' NASA LaRC. In *28th AIAA Applied Aerody-*  
938 *namics Conference, Fluid Dynamics and Co-located Conferences*, Chicago,  
939 Illinois, June 2010. AIAA. DOI: 10.2514/6.2010-4394.
- 940 [48] D.D. Vicroy, K.C. Huber, T.D. Loeser, and D. Rohlf. Low-speed Dynamic  
941 Wind Tunnel Test Analysis of a Generic 53° Swept UCAV Configuration.  
942 In *32nd AIAA Applied Aerodynamics Conference, AIAA Aviation*, Atlanta,  
943 Georgia, June 2014. AIAA. DOI: 10.2514/6.2014-2003.
- 944 [49] D.D. Vicroy, K.C. Huber, A. Schütte, M. Rein, J.P. Irving, G. Rigby, T.  
945 Löser, A-R. Hübner, and T.J. Birch. Experimental Investigations of a  
946 Generic Swept Unmanned Combat Air Vehicle with Controls. *Journal of*  
947 *Aircraft*, 55(2):475–501, 2016. DOI: 10.2514/1.C033782.
- 948 [50] D.D. Vicroy, T.D. Loeser, and A. Schütte. Static and Forced-Oscillation  
949 Tests of a Generic Unmanned Combat Air Vehicle. *Journal of Aircraft*,  
950 49(6):1558–1583, 2012. DOI: 10.2514/1.C031501.
- 951 [51] Y. Yi, T. Hu, P. Liu, Q. Qu, G. Eitelberg, and R.A.D. Akkermans. Dy-  
952 namic lift characteristics of nonslender delta wing in large-amplitude-  
953 pitching. *Aerospace Science and Technology*, 105:105937, 2020. DOI:  
954 10.1016/j.ast.2020.105937.